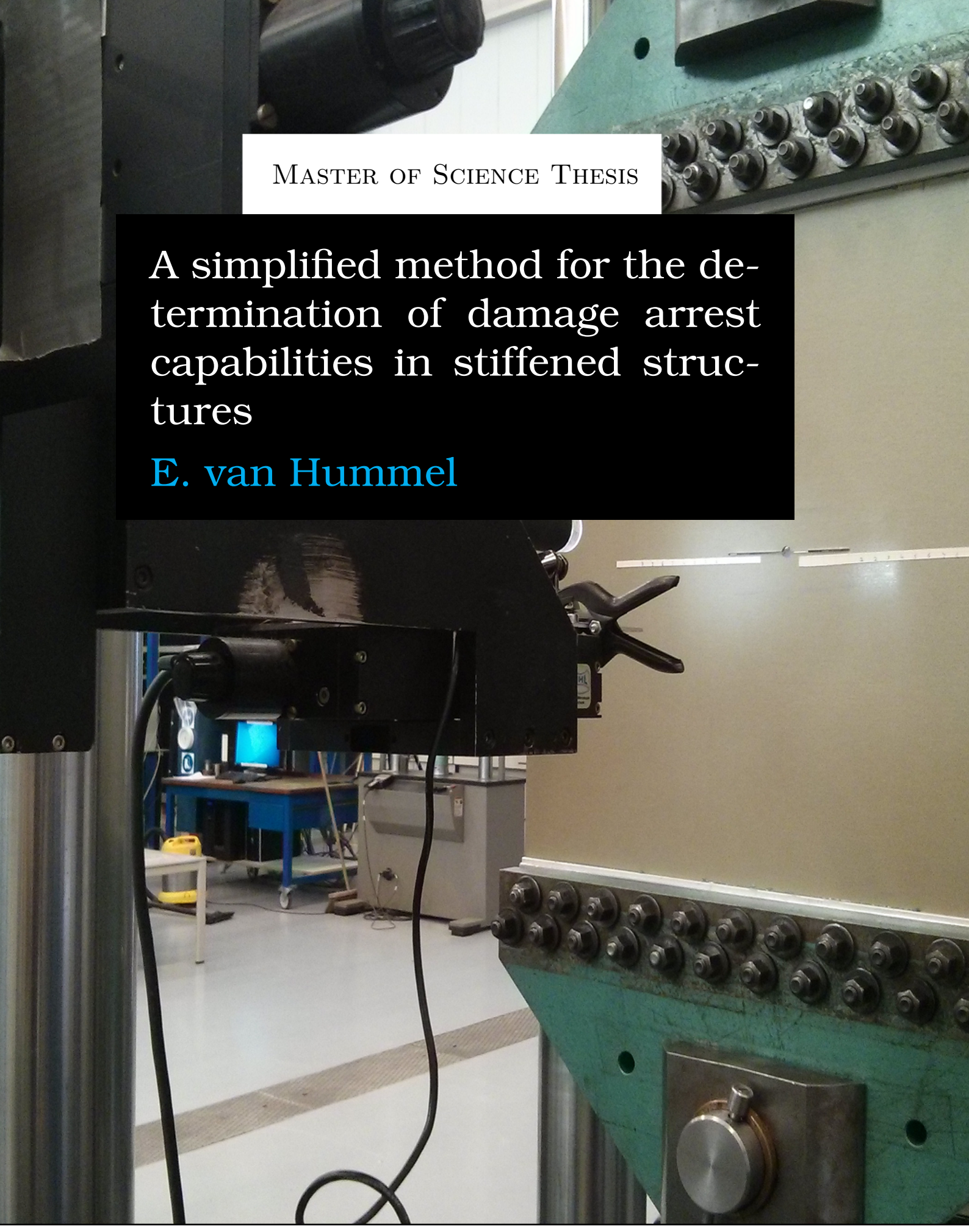

Master of Science Thesis

A simplified method for the determination of damage arrest capabilities in stiffened structures

E. van Hummel

TU Delft Delft University of Technology

Faculty of Aerospace Engineering

A simplified method for the determination of damage arrest capabilities in stiffened structures

Master of Science Thesis

For obtaining the degree of Master of Science in Aerospace Engineering at Delft University of Technology

E. van Hummel

June 30, 2015

Faculty of Aerospace Engineering · Delft University of Technology

Delft University of Technology
Faculty of Aerospace Engineering
Department of Aerospace Structures and Materials

GRADUATION COMMITTEE

Dated: **June 30, 2015**

Chair holder:

Prof. dr. ir. R. Benedictus

Supervisor:

Dr. ir. R.C. Alderliesten

Readers:

Dr. C.D. Rans

F.S. Esrail, MSc

Preface

During my bachelor at the university of Twente I got involved in development of a new student team participating at the Shell Eco-Marathon (SEM). Together with ten fellow mechanical engineering students we founded the Green Team Twente and builded a fuel efficient vehicle to compete in the SEM. In the development of this vehicle I was both responsible for the finance and exterior design, which included the entire production of the composite body. Throughout the project I became increasingly interested in composites due to there potential in future structures and a completely new field of research. Therefore I decided to switch from mechanical to aerospace engineering at the beginning of my master.

The reason I subsequently decided to select this thesis project was based on the practical nature, damage tolerance topic and supervisor. Therefore I want to thank dr. ir. René Alderliesten, who gave me the opportunity to do this project and provided me with valuable feedback during the project.

Throughout my thesis, I am excellent supported by staff and members of the Aerospace Structures and Materials department, who I want to thank for their contribution. A special thanks to Kees, Frans, Bob and Gertjan for their help with the production and execution of the experimental tests. Also a sincere thanks to Raphael Klein for his support during the final phase of my thesis, by giving valuable feedback.

Finally I want to thank my family, friends and especially Fer and Ari who supported me throughout the project, but also provided me with much needed distraction at times. At last I want to specially thank Iris for her much needed love and support during the whole project, without whom I would not have been able to achieve this result.

Delft University of Technology

June 30, 2015

E. van Hummel

Abstract

The recent application of Glass Reinforced Aluminium (Glare) in the Airbus A380 has proven to be a suitable candidate to replace metal structures. The reduction in weight and increased performance results in lower emissions and cost reduction. Therefore research has been performed at the Delft University of Technology, dedicated to the residual strength of fibre metal laminates. This has resulted in reliable prediction methods for flat structures. However in practise these structures are reinforced, to be able to support the loads present in aircraft, while minimising mass.

The addition of these local reinforcement features has revealed interesting residual strength characteristics. It was observed that these structures may possess the ability to arrest unstable crack growth, when damaged, which is of great interest for the analysis of damage tolerance aircraft structures. Currently no simple prediction method is available, giving insight in the crack growth characteristics and enabling crack growth predictions in the early design phase. Therefore the objective of this thesis is to predict the damage arrest capabilities of stiffened structures in a simplified manner.

Based on the literature study it was observed that the current understanding of fibre metal laminate stiffened structures was insufficient for predicting the fracture mechanics of built-up structures. Therefore the available linear elastic fracture mechanics for metal structures is modified to account for plasticity and stiffeners ahead of the crack-tip, by assuming isostrain conditions. As result, the stress intensity reduction factor is successfully implemented, incorporating the presence of a stiffener in combination with the Irwin plasticity correction method. This configuration results in accurate crack growth predictions for residual strength data obtained from literature.

The model verification is expanded with experimental test results to validate the crack-arrest capabilities of a stiffened structure. Therefore four test samples were tested and analysed, representing the different stages of the residual strength diagram. Based on the test results some difference were obtained in the model, which can be appointed to the negligence of stiffener yielding and stiffener effect on the plastic zone growth. Nevertheless a residual strength has been predicted within 7.5 % of the experimental data. Finally it is concluded that the model is able to predict the crack growth characteristics of a stiffened structure in a simplified manner for both metal and fibre metal laminates.

Table of Contents

Glossary

List of Acronyms

Acronym	Definition
FML	Fibre metal laminate
GLARE	Glass reinforced aluminium
FEM	Finite element method
LEFM	Linear elastic fracture mechanics
ARALL	Aramid reinforced aluminium laminate
MVF	Metal volume fraction
FVF_{ld}	Fibre volume fraction in loading direction
DERA	Deutsche Airbus
ASTM	American society for testing and materials
SIRF	Stress intensity reduction factor
SLCF	Stiffener load concentration factor
DASML	Department of aerospace structures and material laboratory
DIC	Digital image correlation
L-T	Longitudinal - transverse direction
T-L	Transverse - longitudinal direction

List of symbols

Symbol	Definition	Subscript	Definition
E	Total energy	s	Surface creation
Π	Potential energy	0	Original situation
W	Work	inf	Infinity
A	Area	xx	x-direction
V	Volume	yy	y-direction
σ	Tensile/Compression stress	xy	Transverse direction
τ	Shear stress	IC	Fracture toughness
ϵ	Strain	I	Initiation, mode I
E	Elasticity modulus	e	Engineering
a	Initial crack length	R	Crack resistance curve
B	Thickness	G	Energy release rate
γ	Atom separation energy	ld	Loading direction
G	Energy release rate	al	Aluminium
ϕ	Airy stress function	fi	Fibres
Z	Westergaard solution to Airy stress	lam	Laminate
	function	res	Residual
z	complex number	eff	Effective
r	radius	$phys$	Physical
θ	radial	$0, 2$	Onset of yielding
K	stress intensity factor	$st, stiff$	Stiffener
ν	Poison ratio	sk	Skin
T	Effective load-carrying fraction	fwc	Finite width correction
α	Residual strength correlation factor	b	Bulging
M	Crack resistance correction factor	$fail$	Failure
W	Width	u, c	Ultimate
t	Thickness		
P	Load		
X	half stiffener pitch		
C	Stress intensity reduction ratio		
L_s	Stiffener load concentration factor		
β	Correction factor		
R	Hoop radius		
χ	Biaxiality ratio		
p	Pressure		
df	Damping factor		
$\bar{y}$	Neutral axis		

Chapter 1

Introduction

Damage to structural components of aircraft is inevitable at some point during the life cycle. Therefore aircraft are designed based on the damage tolerance approach (JAR/-FAR 25) [1]. Large research programs are carried out to develop valuable knowledge related to the processes initiated due to damage. One direction thereof, is the prediction of the residual strength of damaged structures. The locally weakened material may fail resulting in failure of the complete structure. Therefore knowledge of structural design and materials are required to improve the structures of modern day aircraft.

One of the recent trends in the improvement of modern structural components is the replacement of aluminium with Fibre Metal Laminates (FML's) [2]. This material consists of alternating layers of metal and fibre reinforced polymer, can be tailored to a specific set of requirements, by selecting the thickness, amount, orientation and order of the layers. As result both the fatigue life and residual strength characteristics are superior to that of their metal constituent. In the last decades a lot have research has been performed on the best combination of fibres and metals. This has resulted in the application of GLAss REinforced aluminium (Glare) in recent aircraft like the Airbus A380 [3].

The introduction of Glare has resulted in large research programs to describe the fracturing process. Currently the fatigue life and residual strength of flat FML's can be predicted accurately. However following the current trends, research is being performed on the application of local reinforcements in FML structures. The introduction of these reinforcements has resulted in improved damage arrest capabilities and higher fatigue stress levels, enabling the design of even more efficient and lighter structures.

Despite the applications of these local reinforcements in aircraft structures, the justification always requires a curved panel test, as currently no reliable analytical method is able to predict the damage arrest capabilities. The execution of these curved panel tests are always undesired due their time consumption, large size and high costs. Based on these observations a quick and simple method is desired, enabling residual strength predictions in an early design phase as well as giving insight in the crack growth characteristics. Therefore the objective of this thesis is to develop a simple analytical method able to describe the damage characteristics of stiffened structures.

Currently the assessment of these damage features in stiffened structures is analysed using time consuming Finite Element Methods (FEM). In this thesis project the damage characteristics of a stiffened structure is assessed using a developed analytical model based on the Linear Elastic Fracture Mechanics (LEFM). Therefore a Matlab code is written giving more insight in the fracture process.

The report discusses the steps taken to fulfil the objective. First the literature applied in the method is discussed in Chapter 2. This literature is subsequently used in the development of a method given in Chapter 3. Based on this developed model, an experimental program has been designed to validate the results, therefore the design of the experiments and test samples are discussed in Chapter 4. The designed test samples are subsequently tested during a residual strength test. Chapter 5 reflects the results obtained during these tests with the predictions made. Followed by the last part of this thesis consisting of the discussion and verification of the model (Chapter 6) and conclusions and recommendations (Chapter 7).

Chapter 2

Theoretical basis

In the development of new structures for fuselage skins, the trend is to introduce local reinforcements. These reinforcements enable a higher stress level in the structure and introduce damage arrest capabilities. Nevertheless the determination of these damage arrest capabilities is a complex matter. It mainly requires finite element methods to determine accurate answers. The objective of this chapter is to discuss the literature used in the development of a crack arrest method for through-the-thickness cracks, which is able to describe the phenomena in a simplified manner. Therefore it reviews the fracture mechanics developed by Griffith, Westergaard and Irwin [4–6]. Due to the stiffener presence, the stress intensity factor is subsequently modified as proposed by Rans et al. [7]. This, in combination with available crack bulging and finite width correction solutions from literature, describes the literature background [8–12].

2.1 Griffith energy balance

The fracture mechanics as it is known today originates back to the 1920's [4] when Griffith developed a method to predict crack growth. This method used the energy equilibrium proposed by Inglis for a plate with an elliptical hole [6]. Inglis used this energy equilibrium in a linear elastic solution to describe the stress field around an elliptical hole and predicted that the stress would reach infinity for flattened holes.

Based on the analysis of Inglis, Griffith defined his energy equilibrium for a plate containing a centre crack as can be seen in Figure 2.1. He subsequently derived the energy equilibrium as given in Equation 2.1. This equilibrium consists of the potential energy (Π), supplied by internal strain energy and external forces as well as the energy required to create new surfaces (W_s) i.e. work.

$$\frac{dE}{dA} = \frac{d\Pi}{dA} + \frac{dW_s}{dA} = 0 \tag{2.1}$$

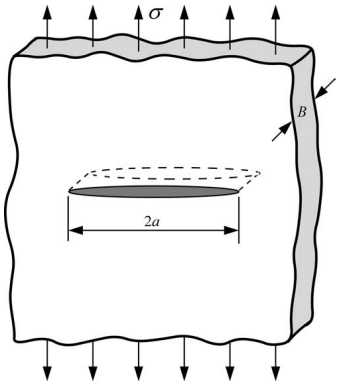

Figure 2.1: An infinite plate containing a through-the-thickness crack subjected to a far field tensile stress [13].

This energy equilibrium states that the creation of an incremental increase in crack area (A) can only be realised when the amount of work is larger than the stored potential energy. The amount of potential energy stored can be determined using the basic principles of work and energy, assuming that a material acts in a linearly elastic fashion [13, 14]. If so Hooke's Law ($\sigma = E\epsilon$) can be used. Applying this relation to the mechanical form of energy, Equation 2.2 can be derived, which represents the potential energy of an isotropic homogeneous volume.

$$\Pi_0 = \frac{\sigma^2}{2E} V \tag{2.2}$$

Considering a plate containing a crack, a reduction in potential energy can be observed. Using the case described by Inglis for an infinitesimal ellipse, it is possible to derive the reduced potential energy for a cracked plate, as given in Equation 2.3, represented by a the reduction in volume (equal to $\pi a^2 B$) [13, 14].

$$\Pi = \Pi_0 - \frac{\sigma^2}{2E} \pi a^2 B \tag{2.3}$$

Next, Griffith determined an expression for the amount of work required to induce crack extension (W_s) by relating it to the energy accompanied with separation of the atoms γ_s over a certain area $2a \cdot B$ as given in Equation 2.4. This subsequently describes the fracture behaviour of an ideally brittle material, which is later on modified by Irwin to account for plasticity enabling the prediction of elastic-plastic materials [13].

$$W_s = 2aB\gamma_s \tag{2.4}$$

Combining the expressions obtained by Griffith, the energy equilibrium equations can be solved. This results in the expression given in Equation 2.5, known as the energy release rate (G). It represents a method to determine crack growth based on the amount of work required.

$$2\gamma_s = G = \frac{\pi \sigma^2 a}{E} \tag{2.5}$$

2.2 Stress field in an infinite plate

Despite the theory developed by Griffith defining a fracture criteria, a solution was desired describing the stress field near the crack-tip, as developed by Westergaard [5]. With this method he was able to describe the stress field in infinite plates containing cracks and developed closed form solutions for 2-dimensional problems, assuming that the material behaves linear-elastic and is loaded in both horizontal and vertical direction with equal magnitude, as can be seen in Figure 2.2.

2.2.1 Airy stress function

The first step in the derivation of the stress field is using the Airy stress functions (ϕ) (given in Equation 2.7) to solve the 2-dimensional equilibrium elasticity problems given in Equation 2.6, where ϕ is any arbitrary function. It can be obtained that regardless the choice of ϕ the equilibrium equations are satisfied, by substituting Equation 2.7 in Equation 2.6. Therefore the stress field can be described using the Airy stress function, by finding an expression for ϕ. One remark is that this is only true if the biharmonic equation is satisfied as well [14].

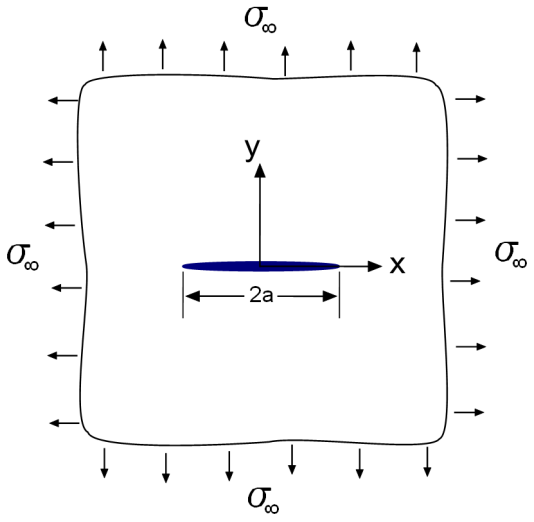

Figure 2.2: Graphical representation of an infinite plate containing a crack [14].

$$\frac{\partial \sigma_{xx}}{\partial x} + \frac{\partial \tau_{xy}}{\partial y} = 0 \tag{2.6a}$$

$$\frac{\partial \sigma_{yy}}{\partial y} + \frac{\partial \tau_{xy}}{\partial y} = 0 \tag{2.6b}$$

$$\sigma_{xx} = \frac{\partial^2 \phi}{\partial y^2} \quad \sigma_{yy} = \frac{\partial^2 \phi}{\partial x^2} \quad \tau_{xy} = -\frac{\partial^2 \phi}{\partial x \partial y} \tag{2.7}$$

2.2.2 Westergaard solution

Westergaard's solution to the Airy stress function enabled the description of stress and strain fields in an infinite 2-dimensional plate containing a crack. His solution is based on the complex numbers $z = x + iy$ and is given in Equation 2.8 [5, 15].

$$\phi = \operatorname{Re}\overline{\overline{Z}} + y \ \operatorname{Im}\overline{Z} \tag{2.8}$$

Where:

$$\frac{d\overline{\overline{Z}}}{dz} = \overline{Z} \quad \frac{d\overline{Z}}{dz} = Z \quad \frac{dZ}{dz} = Z' \quad Z = Z(z) \tag{2.9}$$

Using Cauchy-Riemann equations [14], it was obtained that the Westergaard solution satisfies both the equilibrium equations (Equation 2.6) as well as the biharmonic equation regardless the choice of Z. Westergaard subsequently substituted his solution in the Airy stress functions to determine the stress relations for an infinite 2-dimensional plate, given in Equation 2.10.

$$\sigma_{xx} = \operatorname{Re} Z - y \ \operatorname{Im} Z' \tag{2.10a}$$
$$\sigma_{yy} = \operatorname{Re} Z + y \ \operatorname{Im} Z' \tag{2.10b}$$
$$\tau_{xy} = -y \ \operatorname{Re} Z' \tag{2.10c}$$

The possibility of describing the stress field in an infinite plate regardless the choice of Z enabled Westergaard to develop different solutions. One solution Westergaard obtained, described the stress field of an infinite plate containing a crack while loaded in tension. As result he proposed the following solution [5]:

$$Z(z) = \frac{\sigma_\infty}{\sqrt{1 - \left(\frac{a}{z}\right)^2}} \tag{2.11}$$

In practise the solution obtained by Westergaard can be used to predict the stress state along the crack plane for a tension cracked plate. Therefore the solution is evaluated for $y = 0$ resulting in Equation 2.12. Typical characteristics of this function are the stress singularity occurring at the crack-tip ($x = 0$) and the stress that reduces to the applied stress at infinity, this is visualized in Figure 2.3.

$$\sigma_{xx}|_{y=0} = \sigma_{yy}|_{y=0} = \operatorname{Re} Z = \frac{\sigma_\infty}{\sqrt{1 - \left(\frac{a}{x}\right)^2}} \tag{2.12}$$

Despite the simplicity of the expression obtained, solving the Airy stress function for any other position is a cumbersome process. Therefore Irwin developed a simplified solution, which is able to describe the stress field in the vicinity of the crack-tip. The result of this approximation is included in Figure 2.3 and is discussed next.

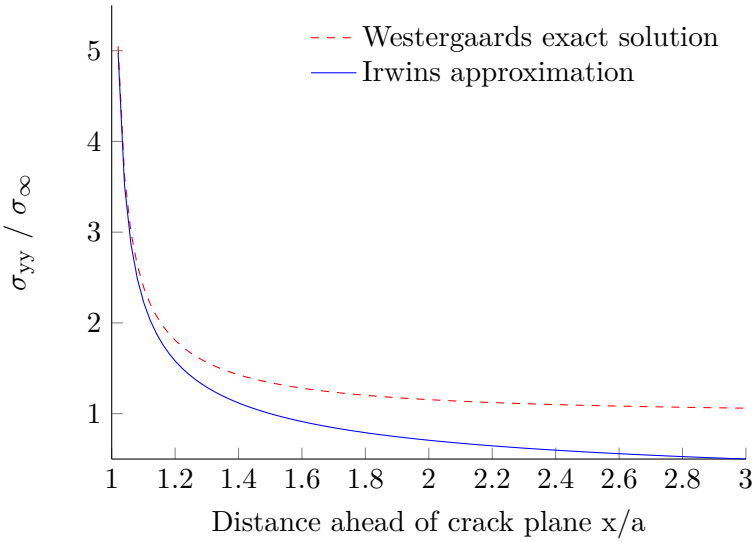

Figure 2.3: Stress field ahead of the crack plane starting at crack-tip ($x/a = 1$).

2.3 Stress intensity factor

The Westergaard solution to the stress field in infinite plates enabled Irwin to develop an approximate solution and has resulted in the origin of the stress intensity factor [13,14]. Irwin showed that the Westergaard solution could be simplified in the area immediately surrounded by the crack-tip ($x/a = 1.1$), as can be seen in Figure 2.3. To do so Irwin substituted the solution for z by a new expression which is a function of polar coordinates and solved the Airy stress functions as described by Westergaard [16]. Therefore he assumed the expression for z given in Equation 2.13, using polar coordinates as can be seen in Figure 2.4.

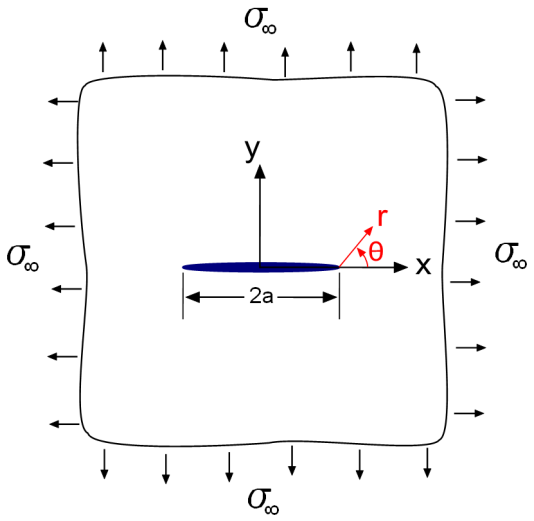

Figure 2.4: Irwin's modification to the Westergaard solution [14].

$$z = a + re^{i\theta} \tag{2.13}$$

The key feature of this new expression is that $r < a$ near the crack-tip, this enabled the discovery of the simplified solution. Assuming that $a^2 >> ar >> r^2$, Irwin ultimately obtained the set of equations given in Equation 2.14, which describes the stress field in the area immediately surrounding the crack-tip.

$$\sigma_{xx} = \frac{\sigma_\infty \sqrt{\pi a}}{\sqrt{2\pi r}} \cos\frac{\theta}{2}\left(1 - \sin\frac{\theta}{2}\sin\frac{3\theta}{2}\right) \tag{2.14a}$$

$$\sigma_{yy} = \frac{\sigma_\infty \sqrt{\pi a}}{\sqrt{2\pi r}} \cos\frac{\theta}{2}\left(1 + \sin\frac{\theta}{2}\sin\frac{3\theta}{2}\right) \tag{2.14b}$$

$$\tau_{xy} = \frac{\sigma_\infty \sqrt{\pi a}}{\sqrt{2\pi r}} \cos\frac{\theta}{2}\sin\frac{\theta}{2}\cos\frac{3\theta}{2} \tag{2.14c}$$

In Figure 2.3 it can be seen that close to the crack-tip, the approximation of Irwin is in close agreement with the exact solution of Westergaard, while further away from the crack-tip the Westergaard solution converges to the far field applied stress and the Irwin solution decreases towards zero. The application of the stress intensity solution, is despite its inaccuracy away from the crack-tip, generally applied in fracture mechanics. The strength of this approximation is that the fracture process is dictated by the stress field close to the crack-tip [14]. It is here the solution provides with a satisfactory answer in a simplified manner and characterises the severity of the stress field, the crack growth direction and failure indication.

Furthermore Irwin identified that the severity of a crack can be related to the term similar in all three equation of Equation 2.14, given in Equation 2.15. This factor is denoted as the stress intensity factor and is used to describe the severity of a crack-load configuration in a flat plate.

$$K = \sigma_\infty \sqrt{\pi a} \tag{2.15}$$

2.3.1 Residual strength prediction

The use of the stress intensity factor has a large contribution in the prediction of fatigue life and residual strength [13, 17]. In the prediction of residual strength the maximal allowable stress intensity factor is denoted as the fracture toughness of a material (K_{IC}). The assumption that a material has a constant fracture toughness enables the construction of a residual strength diagram, as illustrated in Figure 2.5.

In practise the determination of the fracture toughness is complicated as it defines the onset of unstable crack growth. Therefore two additional stress intensity factor are known; the initiation (K_I) and engineering stress intensity factor (K_e). They respectively indicate the onset of stable crack growth and the relation between the initial crack length and ultimate stress of a material [18].

Unfortunately it was observed by Vermeeren and de Vries that the use of the stress intensity factor as a material constant in fibre metal laminates is not suitable [18, 19].

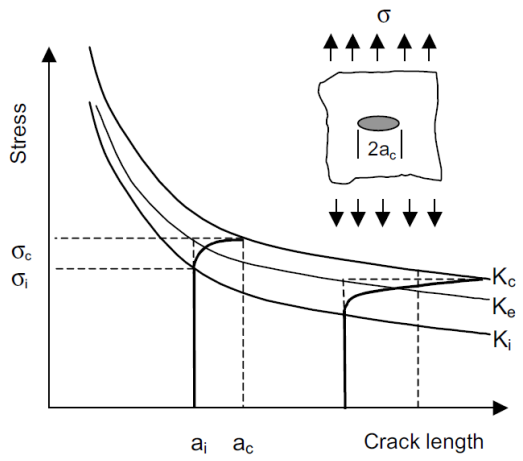

Figure 2.5: Residual strength diagram of a plate containing a centre crack [18].

It was obtained that the value for K_e tends to go to a somewhat constant value as the specimen length increases. However the variance in initial crack length was too large to accept it as material constant. Therefore the application of the stress intensity factor in fibre metal laminates as a single failure parameter is less suitable. It was concluded that the use of the stress intensity factor concept in fibre metal laminates would result in incorrect predictions. In addition Vermeeren also observed that the fracture toughness is even no real constant value for metals [19].

The stress intensity factor concept as material property to determine the residual strength of fibre metal laminates is not suitable due to the large variance in lay-up and width. Nevertheless, it was obtained that the use of the stress intensity factor is still valuable as a relation was determined between the stress intensity and crack resistance curve and is discussed next.

2.3.2 Relation between the stress intensity factor and crack resistance curve

The development of the energy release rate (G) and stress intensity factor (K) has resulted in a global and local parameter used in the prediction of the residual strength of structures [4, 20]. The local stress intensity factor describes the stress field in the proximity of the crack-tip, while the energy release rate represents the potential energy required for crack extension. It was obtained that when comparing both methods a unique relation exist [13]. Therefore both solutions for a linear-elastic material containing a centre-crack are used to derive Equation 2.16. This relation indicates that the local effects can be related to global material behaviour for flat plates. Following this discovery it was Irwin who proved that this relation is valid for all linear elastic mode I crack configurations by performing a crack closure analysis [13, 16].

$$G = \frac{K^2}{E'} \tag{2.16}$$

Where E' is equal to E for plane stress and $E/(1-\nu^2)$ for plane strain. The relation obtained by Irwin provides the link between the local stress intensity and the global

material behaviour. Using this relation it is possible to determine stable crack growth until failure, illustrated with Figure 2.6. Here both the crack resistance curve and stress intensity curve are drawn, the intersection point of both curves are subsequently indicated with A and B and represent stable crack growth with increasing load. When the material is subsequently loaded further to point C, unstable crack growth will occur. The onset of this unstable crack is represented by the tangent point of both curves. At this load the material resistance i.e. potential energy, is equal to the amount of work and can be described by the boundary conditions given in Equation 2.17. Any load or crack increase will result in unstable crack growth. Based on this observation it can be concluded that the tangent point is affected by the shape of the crack resistance curve and initial crack length. It was subsequently Krafft et al. suggesting that the crack resistance curve must be invariant for given sheets thickness [18, 21]. Implying that the crack resistance curve slope is independent of initial crack size.

$$\frac{\partial K_G}{\partial a} = \frac{\partial K_R}{\partial a} \tag{2.17a}$$

$$K_G = K_R \tag{2.17b}$$

Furthermore the shape of the crack resistance curve is related to the type of material. Characterised by for example a vertical crack resistance curve for ideal brittle material representing no stable crack growth until failure [13] to an exponential shaped curve for elastic-plastic behaving materials like metals [18, 19].

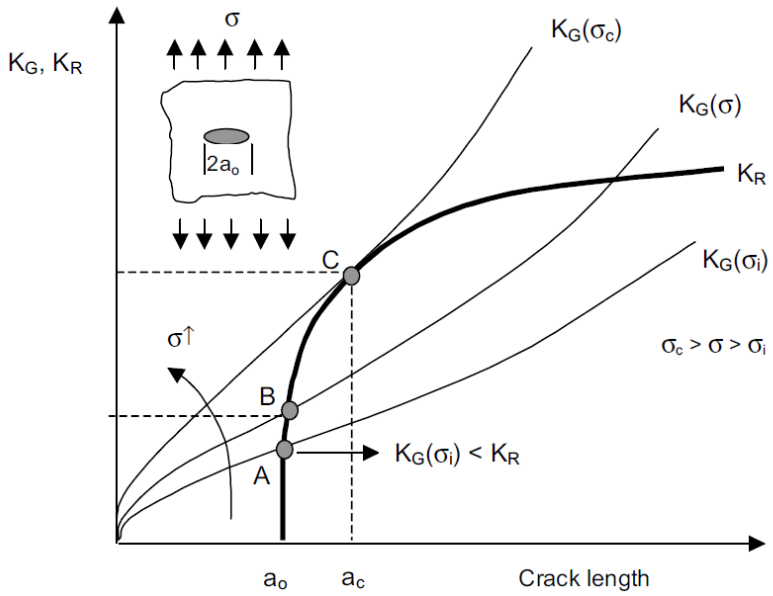

Figure 2.6: Schematic representation of the crack resistance curve (K_R) and stress intensity factor (K_G) for centre cracked plates [18].

2.4 Crack resistance curve of fibre metal laminates

The application of the crack resistance curve in fibre metal laminates is initially proposed by Zaal. He identified the usefulness of the crack resistance curve as residual strength prediction method [22]. Subsequently De Vries developed a general method for Glare [18] and obtained a relation between the amount of metal and fibres in load direction in the material. Using this method it is possible to predict the residual strength of any Glare laminate within the validity range of Table 2.1.

Additional to the applicability of the crack resistance curve for fibre metal laminates it was observed that the presence of the fibres alters the shape of the curve. The crack resistance curve for a single aluminium alloy depends only on the type of alloy and initial crack length, as discussed by Kraft et al. [21], while the determination for fibre metal laminates is more complicated. Therefore De Vries performed research on the factors affecting the crack resistance curve of aluminium 2024-T3 by the presence of glass fibres [18] and concluded that the altered shape could be appointed to:

- the amount of aluminium in the laminate,
- the material properties of the metal layers,
- the rolling direction of the metal sheets compared to the loading direction,
- the amount of fibres in the laminate in loading direction,
- the material properties of the fibre layers and
- the interface between the different layers.

It was observed that the fibres perpendicular to the loading direction do not add any strength to the material. He therefore neglected the fibres in perpendicular direction and divided the remainder of the fibre metal laminate into two separate components, representing the metal layers and fibre layers in loading direction. This enabled him to define a new parameter T representing the effective load-carrying fraction of the laminate, given in Equation 2.18.

$$T = \alpha \cdot FVF_{ld} + MVF \tag{2.18}$$

$$MVF = \frac{t_{al}}{t_{lam}} \tag{2.19}$$

$$FVF_{ld} = \frac{t_{fi,ld}}{t_{lam}} \tag{2.20}$$

Where α is experimentally obtained, the metal volume fraction (MVF) is given by Equation 2.19 and fibre volume fraction (FVF_{ld}) is given by Equation 2.20. Using this new parameter (T) a second order polynomial relation could be obtained between the effective load-carrying fraction (T) and the residual strength illustrated in Figure 2.7. Therefore the curve fit equation given in Equation 2.21 is used, resulting in the constants given in Table 2.1. Finally, a relation is determined between the crack resistance curve

of a fibre metal laminate and the related metal (M), by means of Equation 2.22. This combined with the crack resistance curve of the aluminium constituent ultimately results in the crack resistance curve of the fibre metal laminate, given in Equation 2.23.

$$\sigma_{res} = a \cdot T^2 + b \cdot T + c \tag{2.21}$$

$$M(T) = \frac{a \cdot T^2 + b \cdot T + c}{a + b + c} \tag{2.22}$$

$$K_{r,FML} = M \cdot K_{r,2024-T3} \tag{2.23}$$

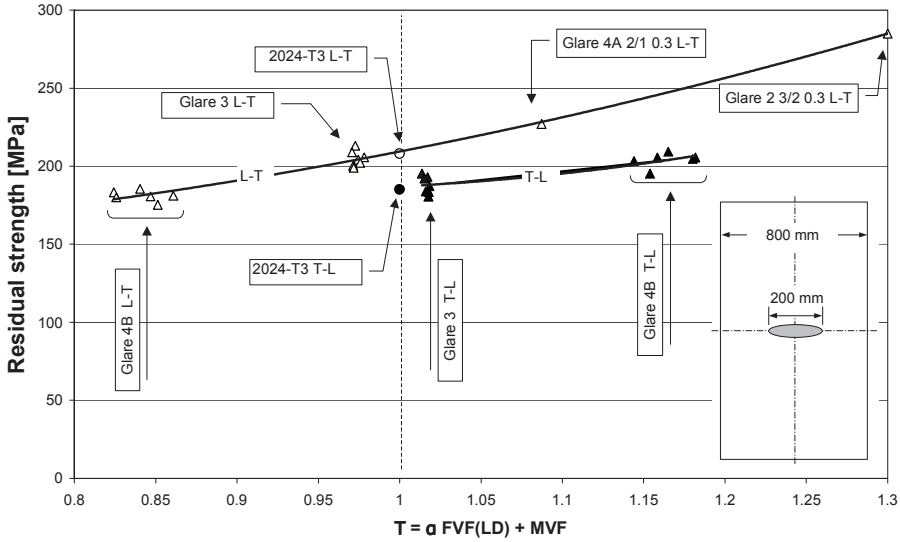

Figure 2.7: Residual strength as function of the effective load-carrying fraction [18].

Direction	α	a	b	c	validation range (T)	source
Glare L-T	1.84	164	-125	171	0.82-1.3	De Vries [18]
Glare T-L	2.1	307	561	441	1.02-1.18	
Glare L-T	1.84	0	189	21	0.6-1.35	Ypma [23]
Glare T-L	2.1	0	147	37	0.6-1.45	

Table 2.1: Validity range and curve fit constant of determined by De Vries and Ypma for aluminium 2024-T3 [18, 23].

In an ideal situation it is desired to use a crack resistance curve of the metal with an equal thickness of the aluminium layers used in the a fibre metal laminate [18]. This can be appointed to the changing fracture mechanics of metals with increasing thickness, due to the transition from plane stress to plane strain conditions [23]. However in practise no data is available for all different metal thicknesses used in the Glare grades. Fortunately De Vries obtained that the difference in crack resistance curve for aluminium 2024-T3 with thicknesses varying between 0.8 mm and 2.0 mm are within scatter [24]. Enabling the use of a single crack resistance curve for all thin laminates as long as plane stress conditions are applicable.

Besides the variation in thickness, a wide specimen should be used to maximise the validity range of the curve. Therefore De Vries based his prediction method on the crack

K_r	k	l	m	n	validity range	source
2024-T3 L-T	16.12	-1.06	27.53	0.612	$W = 2000\ mm$	DERA [25]
2024-T3 T-L	18.08	-0.51	21.49	0.52	$t = 1.6\ mm$	

Table 2.2: Curve fit constants for aluminium 2024-T3.

resistance curve provided by DERA, which is based on 2000 mm wide specimens [25]. They report the curve fit given in Equation 2.24 for aluminium 2024-T3 using the values of Table 2.2. Combining both the crack resistance curve provided by DERA and the prediction method developed by De Vries, the result illustrated in Figure 2.8 can be obtained. Finally it is important to note that these curves already account for plasticity in the wake of the crack for flat plates by means of either the compliance or Irwin method. An explanation for this phenomenon is discussed in Section 2.5.

$$K_{r\ 2024-T3} = k \cdot \Delta a_{eff}^{n} + l \cdot \Delta a_{eff} + m \tag{2.24}$$

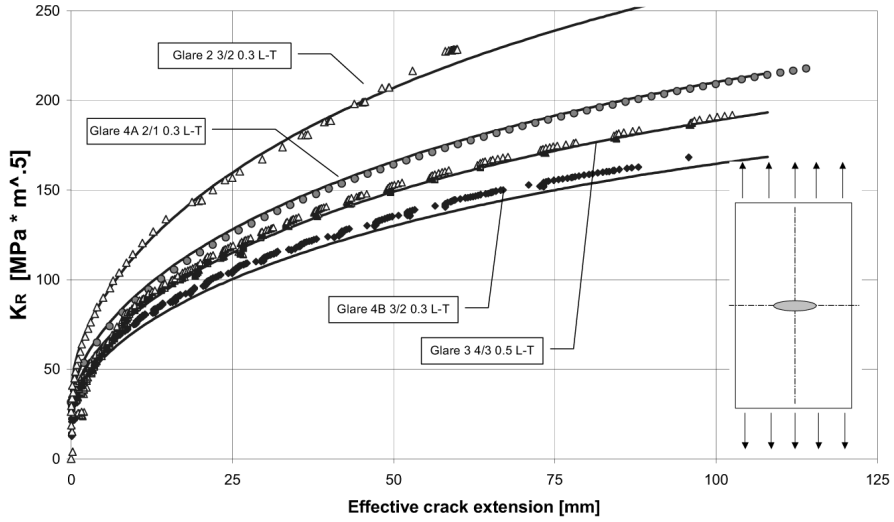

Figure 2.8: Crack resistance curve prediction for different Glare laminates [18].

Following the research performed by De Vries additional experiments where done to validate the method. Ypma verified some of the work performed by De Vries and extended the validity range [23]. He concluded that despite a lack of accuracy in the test results, the method developed by De Vries can be applied. Subsequently Ypma proposed a linear regression, given in Table 2.1, instead of a second order polynomial as the reduction in error was negligible ($\pm 0.1\%$). Figure A.1 and A.2 illustrate the difference in curve fits for respectively parallel (L-T) and perpendicular (T-L) to the rolling direction of the aluminium.

2.5 Plasticity correction

The crack resistance curve theory discussed so far, assumes a linear-elastic material. However, in practise this assumption does not hold for metals. Instead plasticity is induced in the region very close to the crack-tip, which indicate that the stress locally exceeds the yield stress of the material [13, 26]. Therefore the physical crack should be corrected for the presence of plasticity.

2.5.1 Irwin plasticity correction

Irwin was one of the first to identify the locally induced plasticity in front of the crack-tip [27]. He subsequently states that the linear elastic analysis is still true as long as the plastic zone size is small compared to the physical crack length. Following this theory instead of a physical crack length an effective crack length should be used, accounting for plasticity, defined as:

$$a_{eff} = a_{phys} + r_y \tag{2.25}$$

Where the plastic zone size (r_y) should be determined. In practise the determination of the the size and shape of the plastic zone is largely influenced by material type, loading etc. [28]. Nevertheless Irwin simplified the problem and used his stress intensity approximation for the stress field near the crack-tip, as discussed in Section 2.3, to develop a solution for the plastic zone size [13, 14]. Therefore he assumed that the plastic zone has a circular shape with radius r_y and solved Equation 2.14a for $\theta = 0$. By substituting the yield stress ($\sigma_{0,2}$) in this equation he was able to determine Equation 2.26.

$$r_y = \frac{1}{2\pi}\left(\frac{K_I}{\sigma_{0,2}}\right)^2 \tag{2.26}$$

The solution Irwin obtained causes a truncation of the stress at the yield stress illustrated in Figure 2.9. This is not in agreement with the physical understanding of the fracture process. In practise the stresses are redistributed away from the crack-tip in order to satisfy equilibrium. Therefore a second-order approach was proposed by solving a force balance resulting in a plastic zone twice the size of the elastic solution represented by the elastic-plastic solution in Figure 2.9 [13]. As both the stress intensity factor and plastic zone size are a function of the effective crack length, becomes the determination of both parameters an iterative process.

2.5.2 Compliance method

A second method predicting the plastic zone is the compliance method and is described in ASTM E561 [29]. The method uses the increased flexibility of the test specimen caused by the presence of a crack and is valid as long as no non-linearities can be observed in the stress field. Then the compliance method represents a relation between the crack opening displacement and effective crack length, given in Equation 2.27.

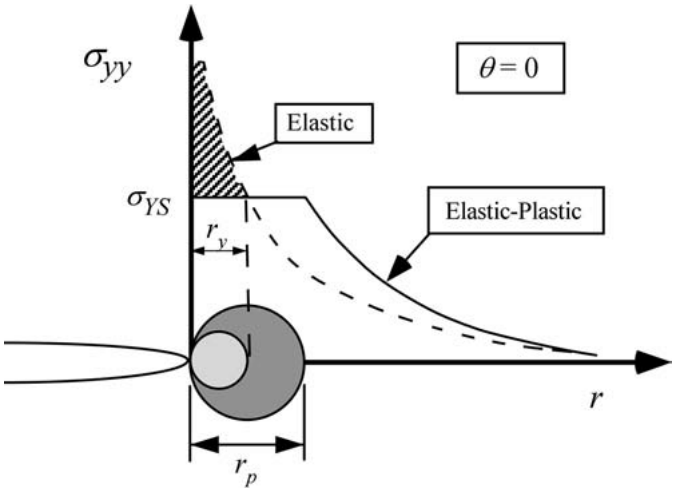

Figure 2.9: Irwin's representation of the plastic zone for both the elastic and elastic-plastic solution [18].

$$\frac{E\ [\nu]}{\sigma\ W} = \frac{2Y}{W}\sqrt{\frac{\pi a/W}{\sin(\pi a/W)}}\left[\frac{2W}{\pi Y}\cosh^{-1}\left(\frac{\cosh \pi Y/W}{\cos \pi a/W}\right) - \frac{1+\mu}{\sqrt{1+\left(\frac{\sin \pi aW}{\sinh \pi Y/W}\right)^2}} + \mu\right] \tag{2.27}$$

E	Young's modulus, N/mm^2
ν	center opening displacement at centre hole, mm
σ	remote stress, P/Wt, N/mm^2
P	load, N
t	specimen thickness, mm
W	total specimen width, mm
Y	half span of gauge to measure ν, mm
a	half crack length, mm
μ	Poisson's ratio

and is valid for: $0.2 < \frac{2a}{W} < 0.8$; $\frac{Y}{W} \leq 0.5$ and $L \geq 1.5W$

One of the benefits of this solution is that it represents the physical process more accurately. The Irwin plasticity correction is solely based on the stress intensity factor and indicates a plasticity growth at load initiation, while the compliance method predict a plastic zone growth at stresses the plastic zone is induced. The drawback of this method is that determination can only be done experimentally or by predefined curves [18].

2.6 Stiffener presence

In the literature discussed so far, flat panels are considered while the objective of this thesis is to predict the crack arrest capabilities of stiffened structures. Therefore the influence of stiffeners on the crack growth characteristics should be taken into account,

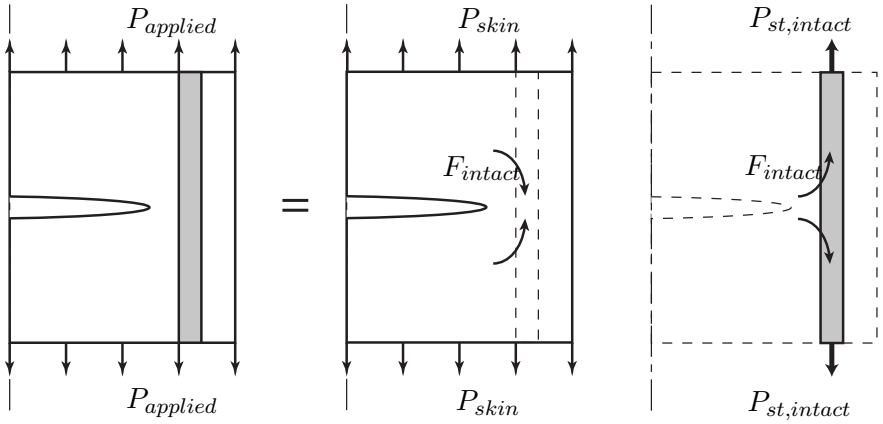

Figure 2.10: Load transfer from skin to stiffener in the presence of a crack (figure adapted from [7]).

by correcting the stress intensity factor. Based on this observation Rans et al. proposed a method, which determines the stress intensity reduction as function of the elastic properties and panel dimensions [7]. Therefore the assumption is made that the material behaves linear-elastic in combination with displacement compatibility between the panel and stiffener. Subsequently the Westergaard solution is used to determine the stress intensity reduction [5].

The unknown variable in this problem is the stress in the skin. The presence of the stiffener alters the stress in the skin and induces load transfer to the stiffener, as illustrated with Figure 2.10. The amount of load transferred to the stiffener is related to the crack size, geometry and elastic properties of the skin and stiffener and is accompanied with complex load redistributions between the stiffener and the skin. Accurate analysis of the process occurring at the interface between the skin and stiffener requires computational solutions, which are also able to incorporate the bond interface.

Adversely to this Rans et al. determined a simplified solution disregarding the local effects and assuming that the far field loads are in equilibrium with the stress ahead of the crack-tip i.e. isostrain between skin and stiffener [7]. This enables the determination of a solution without taking into account the interface between the stiffener and skin ahead of the crack. Additionally he simplified the stiffener geometry to a rectangular cross section with an effective thickness, neglecting the local effects cause by the stiffener geometry.

The stress ahead of the crack-tip for the skin and stiffener is written in terms of the Westergaard solution, respectively given in Equation 2.12 and 2.28, while the far field loads are known.

$$\sigma_{yy,st} = \frac{E_{st}}{E_{sk}} * \frac{\sigma_{sk}}{\sqrt{1-\left(\frac{a}{x}\right)^2}} \quad for \ \left(X_{st} - \frac{W_{st}}{2}\right) \leq x \leq \left(X_{st} + \frac{W_{st}}{2}\right) \tag{2.28}$$

Since both the far field loads and local stresses should be in equilibrium, it is possible to determine the stress in the skin. This is done by integrating the Westergaard solution over the net section of the panel and compared with the far field loads (Equation 2.29). The expression obtained consists of one unknown, the stress in the skin, ahead of the crack-tip. Rearranging the terms ultimately results in the expression required for the stress in the skin as can be seen in Equation 2.30.

$$P_{sk} + P_{st} = \int_a^W \sigma_{yy,sk}\ t_{sk}\ dx + \int_{W_{st}} \sigma_{yy,st}\ \left(\frac{A_{st}}{W_{st}}\right)\ dx \tag{2.29}$$

$$\sigma_{sk} = \frac{P_{sk} + P_{st}}{\int_a^W \frac{t_{sk}}{\sqrt{1-\left(\frac{a}{x}\right)^2}}\ dx + \int_{W_{st}} \frac{E_{st}}{E_{sk}}\frac{A_{st}}{W_{st}} * \frac{1}{\sqrt{1-\left(\frac{a}{x}\right)^2}}\ dx} \tag{2.30}$$

Where the separate loads taken by the skin and stiffener can be determined using Equation 2.31. Rans et al. uses the superposition principle to expand the solution to multiple stiffeners ahead of the crack. Therefore the second integral is solved for every stiffener and the total load contribution is determined by summation of the separate stiffeners [7].

$$P_i = P_{applied}\frac{(EA)_i}{\sum_{j=1}^{n}(EA)_j} \tag{2.31}$$

By substituting the solution obtained by Rans et al. in the stress intensity equation (Equation 2.15) it is possible to determine the stress intensity factor for stiffened structures. Vlieger subsequently defines the stress intensity reduction ratio C as given in Equation 2.32 [30]. Using this definition Rans et al. compared his result with experimental data derived by Schijve and obtained the correlation illustrated in Figure 2.11 [31].

$$C = \frac{K_{stiffened}}{K_{unstiffened}} \tag{2.32}$$

2.6.1 Stiffener load concentration factor

Analogous to a reduction in stress intensity factor due to the presence of a stiffener, a larger stiffener load can be expected. This load concentration in the stiffener induced by a crack can cause the stiffener to fail. Therefore it is of interest to determine the influence of the crack on the stiffener. This is done by defining the stiffener load concentration factor, given in Equation 2.33.

$$L_s = \frac{P_{st} + F_{st}}{P_{st}} \tag{2.33}$$

Where P_{st} is the far field load in the stiffener and F_{st} is the load increase given in Equation 2.34. The unknown skin stress is subsequently determined using Equation 2.30.

$$F_{st} = P_{sk} - \sigma_{sk}\ W_{sk}\ t_{sk} \tag{2.34}$$

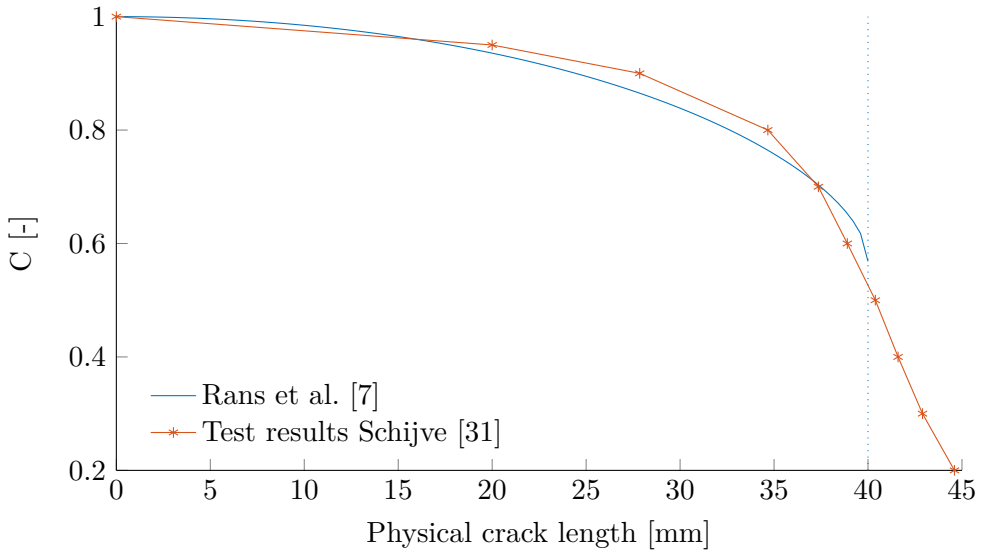

Figure 2.11: Stress intensity reduction ratio prediction for panel design of Schijve [31] $E_{sk} = E_{st} = 71.8\ GPa$, $A_{sk} = 160\ mm^2$, $A_{st} = 100\ mm^2$, $t_{sk} = 1\ mm$, $t_{st} = 4\ mm$ and $X_{st} = 52.5\ mm$.

The application of this stiffener load concentration is used in the assessment of stiffener failure. Nesterenko describes the reduction in ultimate strength of the stiffener by dividing the maximal allowable stiffener stress to the stiffener load concentration factor for an isotropic material [32, 33]. This way he is able to compare the allowable stress with the predicted stress. Stiffener failure can subsequently be obtained at the intersection point of both curves.

2.7 Finite width

The theories discussed in the previous sections are determined for infinite plates, i.e. the crack dimensions are small compared to the plate dimensions. However in practise this assumption is not valid, the stress distribution and crack-tip characteristics are affected by the presence of nearby boundaries [13, 34]. Therefore additional research has been performed on the influence of finite width on the stress intensity factor.

As result numerous expression can be obtained adjusting the stress intensity factor for different configurations, mainly based on experimental results. However some closed form solution were determined for simple configurations [13,15,35], like the centre cracked plates considered in this thesis. Literature subsequently provides with two finite width corrections. The first correction factor is based on the Westergaard solution as given in Equation 2.12. It states that the situation with and without crack should be in equilibrium, which can be expressed as:

$$2\ \beta_{fwc} \int_{a}^{W_{sk}/2} \sigma_{yy}\ t\ dx = \int_{0}^{W_{sk}} \sigma\ t\ dx \tag{2.35}$$

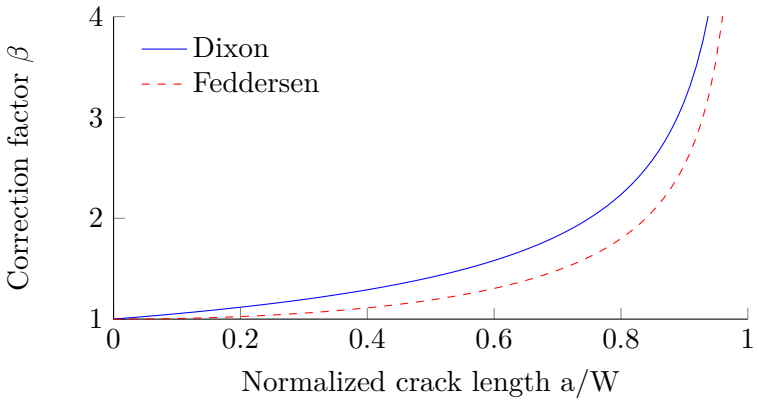

Figure 2.12: Finite width correction factor as function of normalized crack length.

Solving this equation results in the finite width correction factor determined by Dixon (Equation 2.36) [11].

$$\beta_{fwc} = \frac{1}{\sqrt{1 - \left(\frac{2a}{W}\right)^2}} \tag{2.36}$$

A second correction factor in literature has been developed by Feddersen [12]. He discovered the relation based on the experimental data determined by Isida [36] and concluded that the shape could be approximated by Equation 2.37 [37].

$$\beta_{fwc} = \sqrt{\sec\left(\frac{\pi a}{W}\right)} = \frac{1}{\sqrt{\cos\left(\frac{\pi a}{W}\right)}} \tag{2.37}$$

Subsequently the stress intensity solution for an infinite plate should be multiplied with one of the correction factors (β_{fwc}). As both solutions are of the shape $1/(1-x)$ they will increase asymptomatically to infinity and are therefore only valid for approximate $2a/W < 0.9$. The difference between both solutions is illustrated in Figure 2.12.

2.8 Curved panels

Analogous to the consideration for the finite width correction, the analysis is initially performed for flat plates, while the goal of this research is to be able to model finite curved plates. The presence of a curvature causes the crack to deform out of plane as illustrated in Figure 2.13. This strictly means that the crack is not a mode I crack anymore. Instead the crack becomes a combination of a mode I and III crack as illustrated in Figure 2.14. The out-of-plane deformations result in a higher stress intensity induced by the increased degree of freedom of the flanks [8,13]. The combination of a mode I and III crack would imply that mode I analysis as performed in the previous sections is not valid for curved

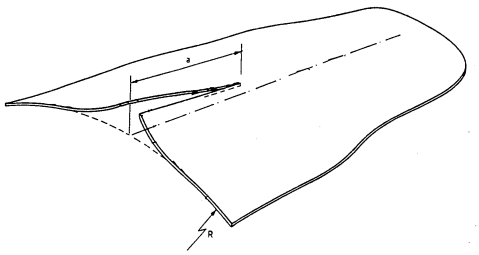

Figure 2.13: Crack bulging due to plate curvature [8].

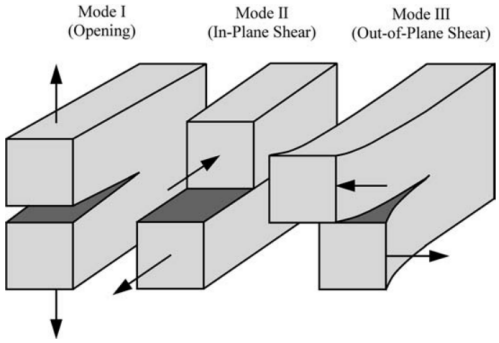

Figure 2.14: Different crack opening modes [13].

plates. Adversely it was obtained that the crack still can be modelled using mode I stress intensity solutions when a correction factor used.

Swift is the first author reporting a correction factor for this matter [9]. He relates the crack bulging contribution to the radius of curvature of the plate, as can be seen in Equation 2.38. This way a constant relation between the stress intensity factor for flat and curved panels is determined. Despite the simplicity of the relation it is still one of the most used correlation factors and compared to the other correction factors sufficiently accurate as can be seen Figure 2.15.

$$\beta_b = 1 + \frac{10a}{R} \tag{2.38}$$

A different crack bulging factor reported in literature, was proposed by Broek et al. [10]. This bulging factor is based on tests of flat and curved panels containing multiple cracks. Using this data he developed a semi-empirical relation given in Equation 2.39.

$$\beta_b = \sqrt{1 + \zeta \left(\left(\frac{E}{\sigma_0} \right) \left(\frac{a}{R} \right)^2 \right)^{2/3}} \tag{2.39}$$

Where the remote stress (σ_0) is equal to the hoop stress for pressurized curved panels, given by; pR/t and the empirical constant (ζ) is equal to 0.671. The last correction factor reported is by Chen et al. He developed a more complex correlation factor as function of the applied pressure in a curved plate. Using the biaxiality ratio ($\chi = \sigma_{long}/\sigma_{hoop}$) Equation 2.40 is obtained, where for an aluminium pressurized fuselage $\chi = 0.24$.

$$\beta_b = \sqrt{1 + \frac{5}{3\pi} \frac{Eta}{R^2 p} \frac{0.316}{\sqrt{1 + 18\chi}} \tanh\left(0.06 \frac{R}{t} \sqrt{\frac{pa}{Et}} \right)} \tag{2.40}$$

Despite the correlation factors obtained from literature, very few is known about the applicability to fibre metal laminates. Chen has performed some fatigue tests on ARALL specimens in 1990 [8] and reports that crack bulging predominantly occurs when fibre failure occurs. When the fibres remain intact the increased bending stresses are fully absorbed resulting in a comparable fatigue crack growth rate to flat plates. In a secondary test Chen performed a residual strength test on an ARALL specimen containing

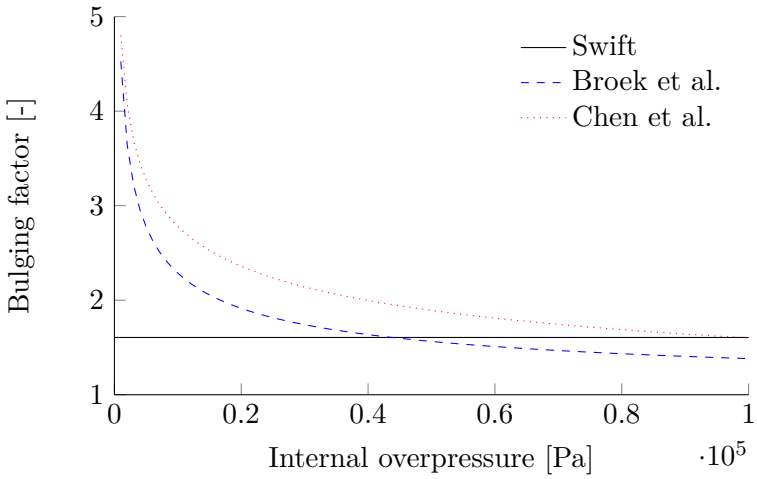

Figure 2.15: Crack bulging correlation factors (R = 1.65 m, t = 1 mm, 2a = 0.2 m, E = 71 GPa, $\chi = 0.24$ taken from [10]).

a large through-the-thickness-crack. Based on this test he suggested that the correlation factor given in Equation 2.40 might work for fibre metal laminates. Since the residual strength ratio between the flat and curved plate was in the same order as the predicted crack bulging factor for the experiment.

2.8.1 Stiffening effect on crack bulging

The discussed literature for curved panels is primarily based on unstiffened panels. The presence of stiffeners in a structure is expected to cause the crack to deform different compared to an unstiffened structure. Similar to the effect of intact fibres in the ARALL specimens of Chen the stiffener may induce a constraint on the amount of out-of-plane deformation of the crack flanks [8]. As result the crack bulging correction might be too high when the crack approaches the stiffener. Therefore Swift proposed a damping factor accounting for the stiffener presence in a two bay crack, assuming the centre stiffener to be intact [9]. He suggests that the contribution of the stiffener on the amount of bulging could be described with a cosine,

$$df = \sqrt{0.5\left(1 - \cos\left(\frac{2\pi a}{L}\right)\right)} \tag{2.41}$$

Where a is the half crack length and L the frame spacing. Subsequently Mor modified the damping factor for symmetric one-bay cracks as can be seen Equation 2.42a [10]. When the crack reaches the stiffener the crack bulging factor is reduced, until zero at the stiffener edge. This ultimately results in the crack bulging solution given in

Equation 2.42b, where β_b is an arbitrary crack bulging solution discussed Section 2.8.

$$df = \sqrt{0.5\left(1 + \cos\left(\frac{2\pi a}{L}\right)\right)} \tag{2.42a}$$

$$\beta_{b,st} = \beta_b \cdot df \tag{2.42b}$$

2.9 Conclusions

Based on the literature discussed, it can be concluded that the application of the crack resistance curve in combination with the modified stress intensity factor should be able to predict the residual strength of a stiffened structure. The stress intensity reduction predicted enhances the physical process occurring at the crack-tip, while the introduction of an effective load-carrying fraction enables the prediction of a crack resistance curve for fibre metal laminates. Combining with additional correction factors accounting for finite width, plasticity creation and crack bulging, the crack arresting capabilities and residual strength predictions of curved stiffened structures looks promising.

Chapter 3

Model development and verification

The literature described in the previous chapter is used in the development of a new method. This method should be capable of describing the fracture process of a stiffened curved structure in a simplified manner. To do so the crack resistance curve method is used in combination with the stress intensity factor, which is subsequently evaluated to determine the crack arrest capabilities and residual strength of a structure. This chapter describes the method developed and verification performed, by means of experimental data retrieved from literature.

3.1 The crack resistance curve

The application of the crack resistance curve in the residual strength prediction method should be able to described the fracturing process as discussed in Section 2.3.2. Therefore the crack resistance curve method developed by De Vries is used [18]. De Vries assumed that the altered shape of the crack resistance curve for fibre metal laminates can be appointed to the contribution of the fibre layers in loading direction and the metal constituent as described in Section 2.4. This method is subsequently applied using the modified curve constants of Ypma and the input crack resistance curve provided by DERA, respectively given in Table 2.1 and Table 2.2. Using this input the crack resistance curve for both loading (L-T) and transverse (T-L) direction can be computed.

3.2 The stress intensity factor for stiffened structures

Following the discussion given in Section 2.3.2, subsequently an expression for the stress intensity factor of stiffened structures should be determined. Due to the presence of stiffeners, the stress intensity factor derived by Irwin is no longer valid as the stress field is locally influenced. Therefore Rans et al. developed a solution for the stress intensity factor including stiffeners as discussed in Section 2.6 [7]. It applies the linear-elastic fracture mechanics and assumes that isostrain conditions will prevail resulting in

a modified expression of the original Irwin stress intensity factor [16]. The expression subsequently determined, replaces the applied stress in the stress intensity factor of Irwin as can be seen in Equation 3.1, representing the stress intensity factor for an infinite plate with a stiffener ahead of the crack.

$$K_{stiff} = \sigma_{sk}\sqrt{\pi a} = \frac{P_{sk} + P_{st}}{\int_a^W \frac{t_{sk}}{\sqrt{1-\left(\frac{a}{x}\right)^2}}\,dx + \frac{E_{st}}{E_{sk}}\frac{A_{st}}{W_{st}}\int_{W_{st}} \frac{1}{\sqrt{1-\left(\frac{a}{x}\right)^2}}\,dx}\sqrt{\pi a} \tag{3.1}$$

Where the required stiffnesses ($E_{sk,st}$) for laminated structures are computed using the classical laminate theory [38]. Subsequently the Stress Intensity Reduction Factor (SIRF) is defined and represents the ratio between the stiffened and unstiffened stress intensity factor (Equation 2.32). The factor indicates the stress intensity reduction due to the stiffener ahead of the crack-tip, as for example illustrated in Figure 3.1. It provides insight in the stiffener effectiveness and enables the comparison between flat plates and stiffened structures in one ratio.

The SIRF curve is subsequently characterised with a ratio of one when no crack is present and decreases with increasing crack length due to a lower stress intensity factor for the stiffened structure. This effect is expected to be present until the stiffener edge, at this point the stiffener cross section will decrease in front of the crack affecting the effectiveness of the stiffener. This results in a stiffener partially bridging the crack and disabling the application of the equation determined by Rans et al. [7], since the second integral term of Equation 3.1 is no longer valid.

$$C = \frac{K_{stiffened}}{K_{unstiffened}} \qquad (\text{ 2.32 revisited})$$

To account for the stiffener bridging the crack, Rans et al. subsequently proposes a compatibility equation forcing equilibrium between the cracked skin and bridging stiffener along the stiffener width [7]. They developed the method initially to predict the fatigue life of metallic structures. In these cases the crack may pass the stiffener without failure of the structure.

Considering the residual strength of stiffened structures it is expected that the structure will fail if the crack is below the stiffener. Therefore it is decided to not implement the compatibility equation. Instead the effective stiffener is considered i.e. the stiffener width is reduced equal to the crack length below the stiffener. This way the reduced effectiveness of the stiffener is captured in a simplified manner by the reduced cross section and maintains the application of the original solution. The effect of this assumption is subsequently illustrated in Figure 3.1. It can be seen that the SIRF indeed becomes less effective and reduces the SIRF as the crack growths beneath the stiffener.

The SIRF is subsequently used in the crack arrest prediction model to account for stiffener ahead of the crack. However as discussed in Section 2.5.1, the stress intensity factor should also be corrected for the plasticity ahead of the crack-tip. Therefore the Irwin plasticity correction is used. It can be applied as long as the plastic zone size is small compared to the crack length [13, 27] and implies an iterative process converging to an

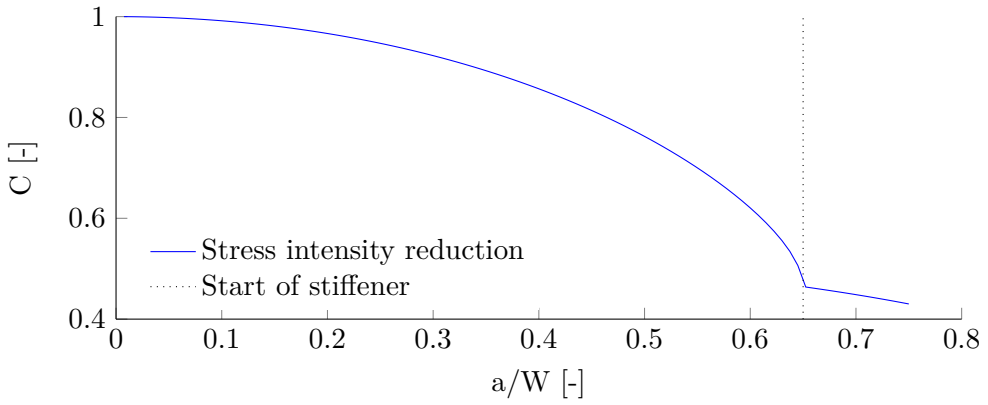

Figure 3.1: Stress intensity reduction factor (SIRF) example, with a stiffener starting at $a/W = 0.65$.

effective stress intensity factor. In this method the SIRF is included in the process, where the SIRF can either be a function of the physical or effective crack length. The trade-off determining the correct crack length is subsequently based on the physical representation. Assuming an effective crack length would imply the negligence of the intact fibres and plastic material in the wake of the crack. This results in an overestimation of both SIRF and crack arrest capabilities of the structures. Opposite to the assumption of the SIRF to be a function of the effective crack length is the physical crack length, which includes the intact fibres and plasticity deformed material in front of the crack. This may result in a more conservative assumption of the SIRF.

In practise the SIRF for an elastic-plastic material will be between both crack lengths, assuming the physical crack length is expected to give a more conservative estimation of the actual SIRF. Therefore it is decided to include the SIRF as function of the physical crack length. Furthermore it is expected that including the SIRF as function of the effective crack length in the Irwin plasticity correction may cause convergence problems when the crack reaches the stiffener due to the iterative process.

Finally the finite width correction and crack bulging solution are applied. The finite width correction is included to account for nearby edges as discussed in Section 2.7. Therefore the Dixon correction based on the Westergaard solution is included in the model [11]. Secondly if a curved panel is analysed, the crack bulging solution could be used to modify the stress intensity factor accounting for the curvature.

Literature subsequently provides with several finite width and crack bulging solutions modifying the stress intensity factor for flat plates, as discussed in Section 2.8. These solutions can all be implemented in the model, where the solution provided by Swift is the most applied and simplest [9, 10]. However these correction factors are developed to account for curvatures in flat plates. The introduction of stiffener increases the complexity and could possibly be captured by a damping factor as discussed in Section 2.8.1.

3.2.1 The stiffener load concentration factor (SLCF)

Similar to the introduction of the SIRF, the stiffener load concentration factor (SLCF) is defined. The analytical solution proposed by Rans et al. enables the determination

of the stress ahead of the crack-tip and in the stiffener. Using this relation it is possible to determine the SLCF (Equation 2.33), which is again a function of the physical crack length similar to the SIRF. Figure 3.2 subsequently illustrates the SLCF related to the example of Figure 3.1.

$$L_s = \frac{P_{st} + F_{st}}{P_{st}} \qquad (\text{2.33 revisited})$$

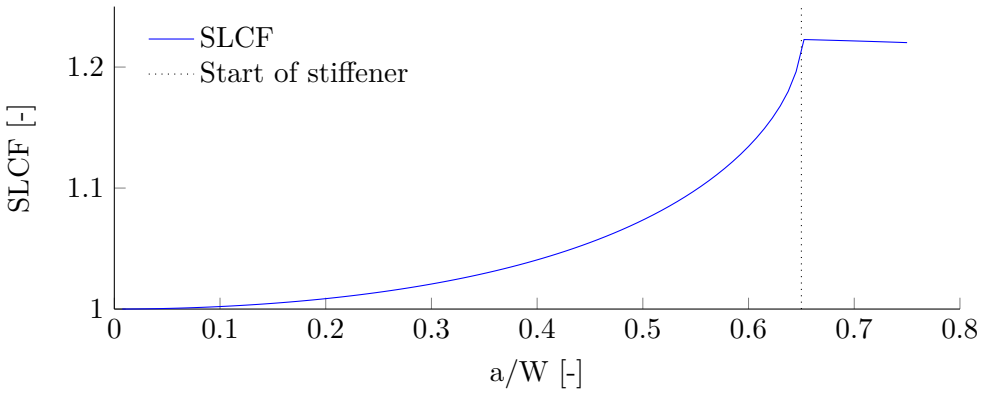

Figure 3.2: SLCF ratio example, with a stiffener starting at $a/W = 0.65$.

The SLCF is subsequently used to artificially modify the failure stress of the material as a function of the crack length, which is used in the assessment of stiffener failure. A crack length of zero would imply a SLCF of one, which indicates that the stress ahead of the crack-tip is equal to the far field stress. Increasing the crack size can either result in an increase or decrease in the SLCF depending on the stiffness and dimensions of both the skin and stiffener and crack length. The decrease in SLCF can be explained by the large stress increase induced close to crack-tip. In theory this can attract load away from the stiffener resulting in a lower SLCF, which will results in a higher applied failure stress compared to maximum allowable stress (note that this is obtained excluding assessing failure of the skin).

3.3 Crack growth predictions

The determination of the stress intensity factor for stiffened structures and the crack resistance curve for fibre metal laminates enables the prediction of the crack growth characteristics. Therefore both solutions should be compared as discussed in Section 2.3.2. Using this method it is possible to identify the three stages present in fibre metal laminates; no crack growth, stable crack growth and unstable crack growth depending on load conditions and crack length as illustrated in Figure 2.6. Based on the identification of these three stages it is possible to construct a crack growth diagram. Therefore at the intersection points the stress is stored, until the stress intensity factor no longer intersects the crack resistance curve [33]. At this point the material resistance is smaller than the amount of work resulting in unstable crack growth.

Additionally to the crack growth diagram, the stress in the stiffener should be determined, to be able to assess stiffener failure. In monolithic structures this stress is equal

to the skin stress as it is constant along the cross section. For structures made of composites or different materials the stresses become different due to the stiffness difference. Therefore the stress in the stiffener must be determined using Equation 3.2, which is based on the isostrain assumption. This stiffener stress vs. crack growth diagram is subsequently combined with the stiffener failure curve to determine stiffener failure. Where the stiffener failure curve can be determined dividing the maximum allowable stress for a material to the SLCF as given in Equation 3.3 [32,33]. Using this method the far field applied stress can be compared with the allowable stress accounting for the elevated stress close to the crack and enabling the assessment of stiffener failure.

$$\sigma_{sk} = \frac{F}{\frac{E_{st}}{E_{sk}} A_{st} + A_{sk}} \quad \sigma_{st} = \frac{E_{st}}{E_{sk}} \sigma_{sk} \tag{3.2}$$

$$\sigma_{fail,st} = \frac{\sigma_u}{L_s} \tag{3.3}$$

3.4 Model structure

The theory elaborated in the previous sections is subsequently combined in a Matlab model. It simulates a residual strength test computing the stress intensity reduction factor, stiffener load concentration factor, crack growth diagram and stiffener failure curve. The model is therefore subdivided into three phases, as illustrated in Figure 3.3. Initially the input is converted into the correct quantities, followed by the failure determination. Finally the model is concluded with the output indicating the failure mode and stress.

In the first phase the selected parameters are converted. Therefore the material properties of the laminate and stiffener, the geometry and initial crack length are required. Based on the input the effective load-carrying fraction (T), elasticity modulus (E), areas (A) and equivalent stiffenesses (EA) are computed. As result the SIRF, the SLCF and the crack resistance curve of the fibre metal laminate are determined.

Now the input parameters are converted in the quantities required to determine the crack growth diagram. The second step then can be performed, indicated as failure determination in Figure 3.3. Here the stress intensity factor of the stiffened structure (K_{stiff}) is combined with the crack resistance curve of the skin (K_r). This results in the construction of the crack growth diagram. Additionally the stiffener failure curve is derived based on the SLCF and failure stress of the material.

Finally the last phase consists of the residual strength prediction of the structure. In the failure determination step, two curves are constructed representing the development of the stress in the skin and failure of stiffener. Based on these results, the residual strength of the structure must be obtained. This implies the determination of the lowest failure stress, where stiffener failure can be identified as the intersection of the stiffener failure curve and the crack growth diagram, accounting for the different stiffener stiffness. The failure of the skin can be identified as the onset of unstable crack growth resulting in no intersection point with the crack resistance curve, as discussed in Section 2.3.2.

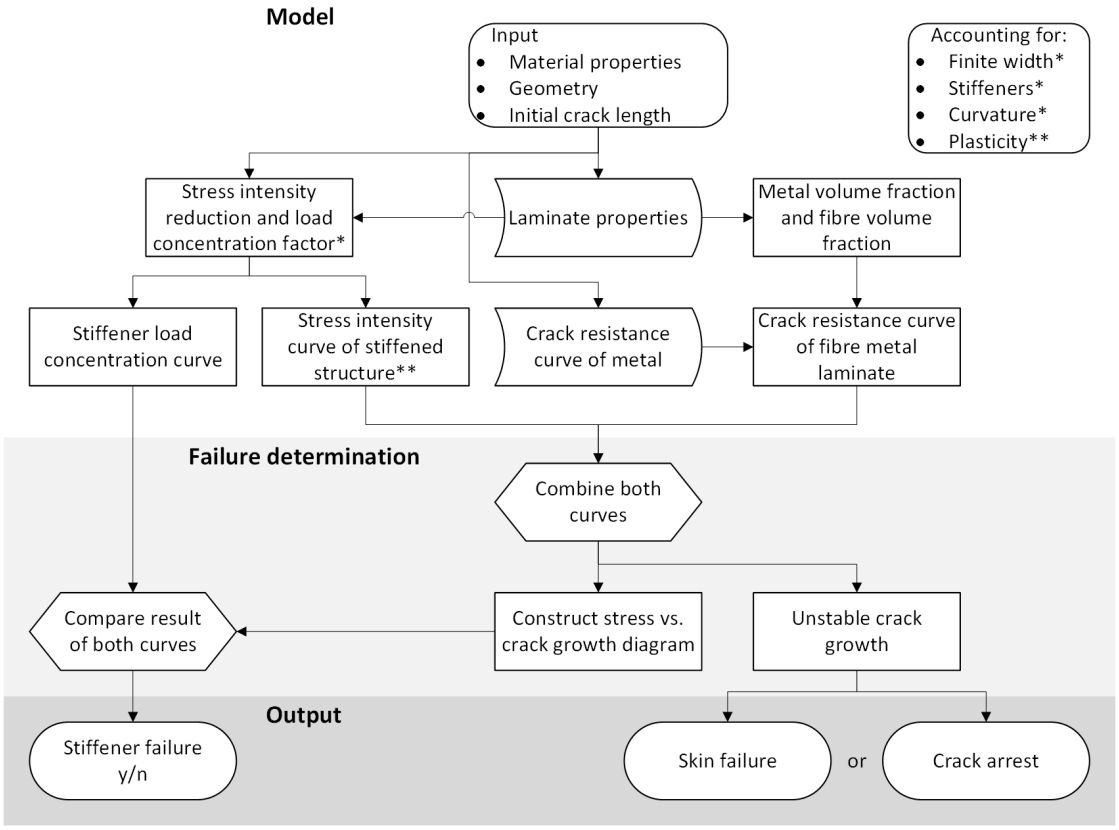

Figure 3.3: Schematic representation of the model structure used in the development of the method.

3.5 Model verification

Following the model development, the results should be verified. Therefore literature is consulted to verify the different steps taken in the model. In this section the available data related to the different aspects is compared with the output of the model.

3.5.1 SIRF and load concentration verification

The developed SIRF solution is validated with available literature, as can be seen in Figure 3.4 and 3.5. In Figure 3.4 Schijve determined the reduction in stress intensity factor for an integral bonded panel made of Al. 2024-T3 [31]. As can be seen in the figure a good correlation between data and model can be obtained until the stiffener. At this point the assumption of an effective stiffener width is initiated. This result in a mismatch, with literature giving a more conservative prediction of the SIRF.

Secondly the model is assessed using the analysis of Vlieger, which is based on a riveted panel [30]. He analysed a stiffened panel consisting of Al. 7075-T6 skin and stiffeners and performed an analytical and FEM analysis by taking the contribution of the first three rivets into account and reports the SIRF. As can be seen in Figure 3.5, a good correlation can be obtained until close to the stiffener. At this point the model assuming

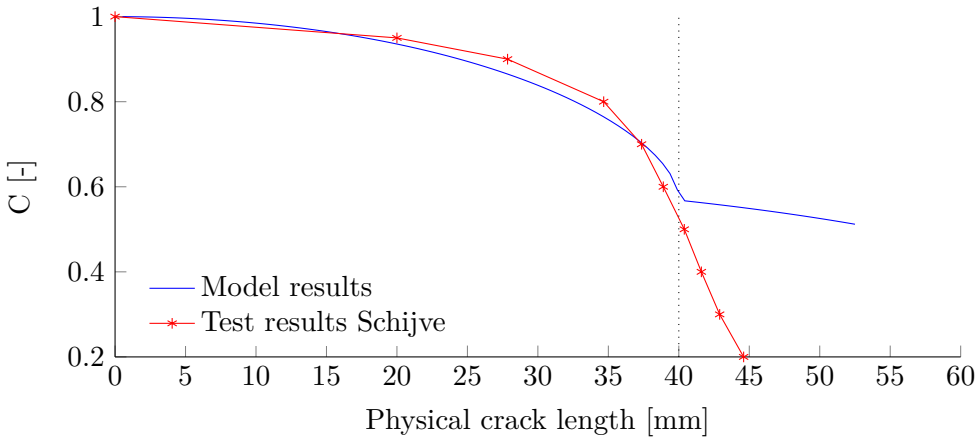

Figure 3.4: Comparison between SIRF test results of Schijve and model prediction [31].

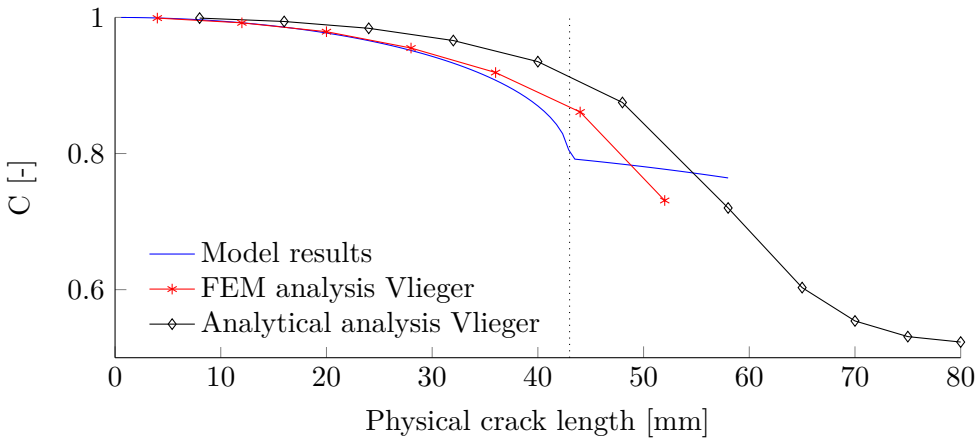

Figure 3.5: Comparison between SIRF analysis results of Vlieger and model prediction [30].

a bonded interface computes a larger SIRF, which can be appointed to the increased load-carrying capabilities of the continuous interface. Despite the mismatch below the stiffener, again the same trend can be identified as for Schijve.

Vlieger also reports the stiffener load concentration as can be seen in Figure 3.6. Again both the analytical and FEM results are compared with the model resulting in a similar conclusion as the SIRF comparison. Here the reduction in SIRF at the stiffener location results in a stagnation of the SLCF increase in the model, levelling the stiffener failure stress. It can be concluded that the model is be capable of describing the problem in a conservative manner in the range required to determine the residual strength of a stiffened structure. Therefore the next verification step was performed, which is the prediction of the residual strength of flat plates.

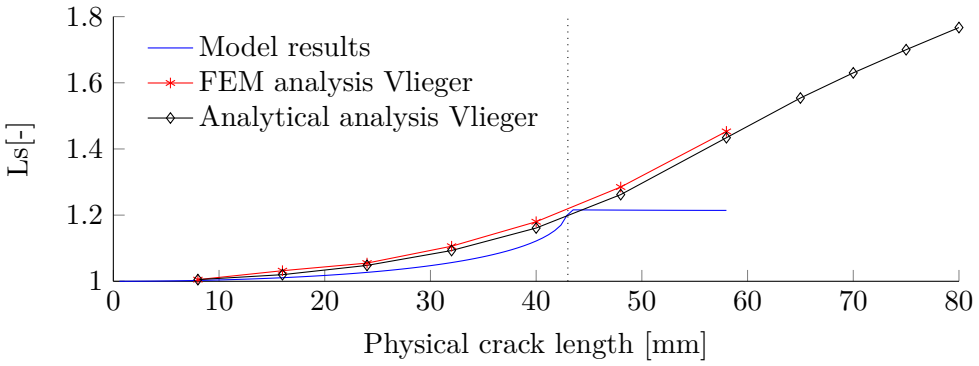

Figure 3.6: Comparison between load concentration analysis results of Vlieger and model prediction [30].

3.5.2 Flat plate verification

Parallel to the verification of the SIRF and SLCF, the residual strength prediction of flat plates is validated. As discussed in Section 3.3 this implies the combination of the crack resistance curve and stress intensity factor. Initially the crack growth characteristics of aluminium panels is evaluated followed by the prediction of Glare panels. Therefore the crack growth model is used, assuming the SIRF and SLCF to be equal to one, enabling the determination of the residual strength of flat plates.

As can be seen in Figure 3.7 a good correlation for aluminium 2024-T3 is obtained between the experimental results and predictions, only a slight offset can be identified during crack initiation. This is induced by the application of the Irwin plasticity correction in the model [27]. This correction determines the effective crack length based on the stress intensity and yield stress. Therefore effective crack growth is initiated immediately after load application, while in practise no crack growth will be visual until close to the crack initiation load. This effect can be identified in the figure by the slight underestimation [18].

After the prediction of the residual strength of the aluminium panel the complete laminate is validated. Therefore the test-matrix of De Vries is used [40]. In a test series, De Vries tested several lay-ups for Glare 3 and 4B in both loading (L-T) and transversal direction (T-L). From this test series subsequently the lowest and highest test results are retrieved and compared with the predictions made for all laminates. As can be seen in Figure 3.8 and 3.9 for respectively Glare 3 L-T and Glare 4B T-L, again a good correlation can be obtained between the experimental data and predictions.

The figures indicate a similar residual strength for all laminates, which can be appointed to the crack resistance curve method. In this method the effective load-carrying fractions are determined for all individual curves, as discussed in Section 2.4. As result a similar effective load-carrying fraction and residual strength is expected for all laminates. This effect is indeed visible in both figures, where a minor difference is still visible for Glare 4B while the Glare 3 predictions are practically equal. The second observation is again a slight underestimation of crack initiation and can be appointed to the use of the Irwin plasticity correction. The remaining figures of Glare 3 T-L and Glare 4B L-T are shown in Appendix C.

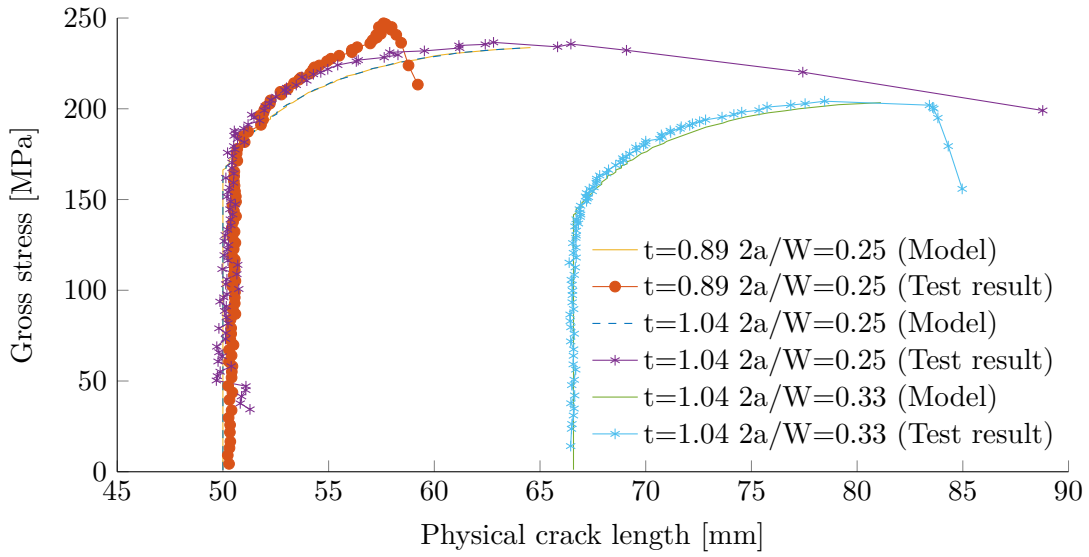

Figure 3.7: Comparison between experimental and predicted results for Aluminium 2024-T3 alloy, W = 400 mm [39].

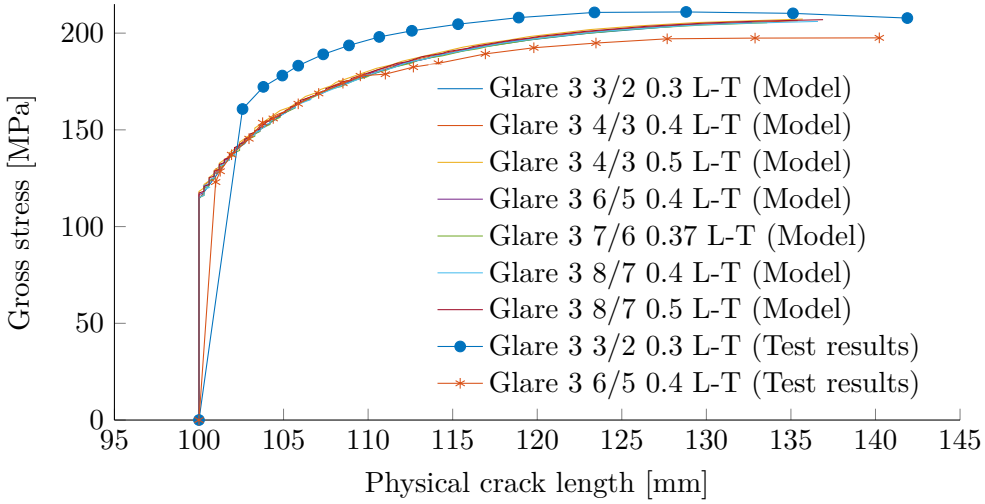

Figure 3.8: Comparison between experimental and predicted results for several Glare 3 L-T grades, W = 800 mm and 2a/W = 0.25 [40].

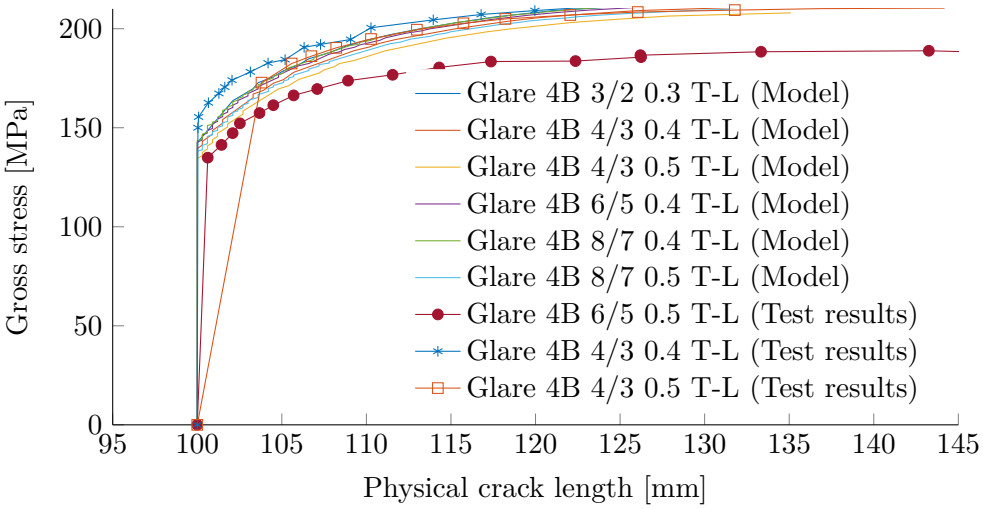

Figure 3.9: Comparison between experimental and predicted results for several Glare 4B T-L grades, W = 800 mm and 2a/W = 0.25 [40].

3.5.3 Stiffened structure verification

The model has proven to compute sufficient accurate result for flat panels to continue the verification process. The final step taken is therefore the verification of fibre metal laminate stiffened structures. The literature related to this subject consists of Glare 3 skins with either an aluminium or Glare doubler. The comparison between the prediction and experimental results are subsequently given in Figure 3.10, 3.11 and Figure C.3. Based on these figures a good correlation of the crack growth behaviour can be obtained.

The model overestimates the residual strength of the aluminium stiffened structure, while predicting a slightly lower residual strength for the Glare stiffened structures. This results in a more conservative prediction. Secondly the influence of the stiffener on the crack growth path increasing the residual strength of the structure is well captured by the model. The SIRF indeed captures the reduction in stress intensity compared to flat plates increasing the residual strength of the structure. Finally the assumption of an effective stiffener width results in a crack extending below the stiffener, supporting the expected fracture path. The results are subsequently summarized in Table 3.1.

Table 3.1: Comparison between experimental data and prediction results.

		Prediction	Test results	Accuracy [%]
Glare 3 3/2 0.2 with	σ_c [Mpa]	235.0	227.9	3.1
Al. 2024-T3 doubler	a_c [mm]	65.0	68.1	-4.6
Glare 3 3/2 0.2 with	σ_c [Mpa]	259.3	270.4	-4.1
Glare 2 2/1 0.2 doubler	a_c [mm]	66.4	69.1	-3.9
Glare 3 3/2 0.3 with	σ_c [Mpa]	255.1	268.4	-5.0
Glare 2 2/1 0.2 doubler	a_c [mm]	66.7	69.0	-3.3

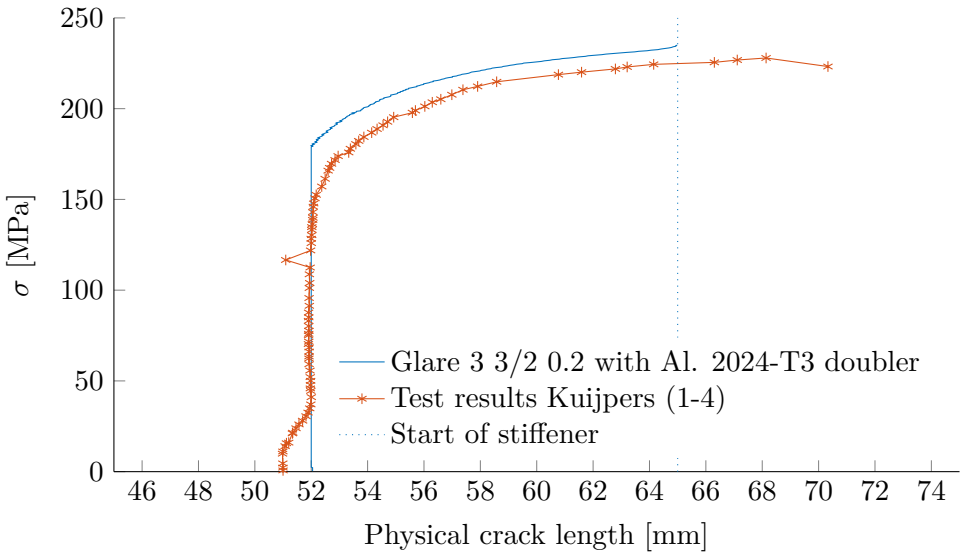

Figure 3.10: Comparison between experimental and predicted results for stiffened structure. skin: Glare 3 3/2 0.2 stiffener: Al. 2024-T3, $W_{sk} = 400$ mm, $W_{st} = 25$ mm, $t_{st} = 0.2$ mm and $2a/W = 0.25$.

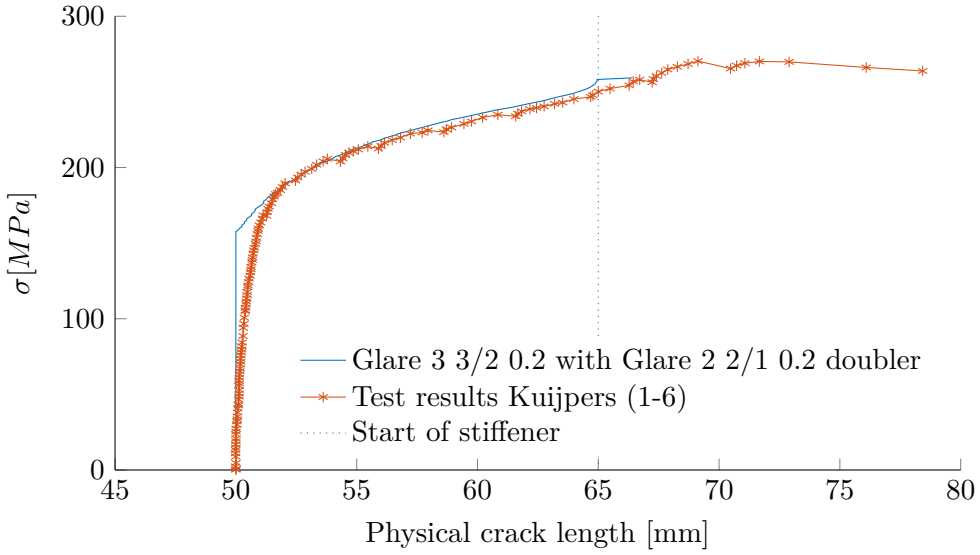

Figure 3.11: Comparison between experimental and predicted results for stiffened structure. skin: Glare 3 3/2 0.2 stiffener: Glare 2 2/1 0.2, $W_{sk} = 400$ mm, $W_{st} = 25$ mm, $t_{st} = 0.65$ mm and $2a/W = 0.25$.

3.6 Conclusions

It can be concluded that the combination of the crack resistance curve and stress intensity factor can be used to predict the residual strength of flat plates. Verification results for flat plates indicate that all predictions correlate well with experimental data obtained from literature. The introduction of the SIRF to account for the stiffener presence is subsequently applied to be able to predict failure of stiffened structures. Based on the verification results it can be concluded that the model is able to describe the difference in crack growth characteristics and predict the residual strength accurately. Ultimately the validity range is given in Table 3.2 and 3.3 for respectively flat and stiffened structures.

Table 3.2: Flat panel validity range of the model.

Flat plates	Metal		Fibre metal laminate	
Material	Al. 2024-T3		Glare 3	Glare 4B
Lay-up/loading direction	L-T		3/2 0.3 L-T	8/7 0.5 T-L
t	0.89	1.04	1.4	6.625
2a/W	0.25	0.33	0.25	
W	400		800	

Table 3.3: Stiffened structure validity range of the model.

Stiffened structure			
Skin	Material	Glare 3	
	Lay-up/loading direction	3/2 0.2 L-T	3/2 0.3 L-T
	2a/W	0.25	
	W	400	
Stiffener	Material	Al. 2024-T3	Glare 2
	Lay-up/loading direction	L-T	2/1 0.2 L-T
	Stiffener width	25	

Chapter 4

Test sample design and preparations

In follow-up of the development of a model, the prediction results are validated by means of experimental tests. The model proved to be capable of predicting the crack growth characteristics accurately for cases obtained from literature as described in Section 3.5. Unfortunately non of these cases show crack arrest before failure while this is the main goal of this thesis. Therefore the objective of this chapter is to describe the development of four test samples and test preparations, used to identify the crack arrest phenomena. These test samples are subsequently subjected to a residual strength tests.

4.1 Test sample design

The design of the test samples is based on previous tests performed by Ypma [41]. In 2003, Ypma performed residual strength tests on large stiffened panels containing two-bay cracks to verify the design tool PCRACKS, which is a computer code developed at the TU Delft [42, 43] and discussed in the literature review [44]. For this he used both Glare 3 5/4 0.4 and Glare 4B 4/3 0.4 as skin material and aluminium 7349 alloy as stiffener material. The design made by Ypma is subsequently used as a baseline for the test samples presented in this thesis and tailored to the present requirements.

4.1.1 Test sample skin selection

The selection of a skin material suitable for the residual strength tests is based on available resources at the TU Delft. It was decided to select a panel out of the current stock, which meets the requirements. As the model is in theory capable of implementing any type of Glare, the requirements are mainly based on production and test facilities available and are enumerated next.

- Minimize panel thickness, to reduce amount of force required during residual strength test
- Panel thickness should have some resemblance with currently used fuselage panels in aircraft
- Minimal panel size or combination of panel sizes all consisting of the same type of Glare should be large enough to be able to produce four panels
- Available in the TU Delft stock
- Quasi-isotropic (preferable Glare 3 and 4) and within the validity range of the model
- Symmetric lay-up

Based on these requirements, it was decided to use Glare 3 5/4 0.3-0.4, which is a non-standard Glare panel. The difference with an ordinary Glare 3 panel is the variation in aluminium thickness through the sheet. Instead of five layers of 0.3 mm, two layers are replaced by aluminium sheets of 0.4 mm in an alternating order, as can be seen in Figure 4.1. Subsequently the stacking sequence of the prepreg layers is mirrored with respect to the mid-plane to achieve a symmetric lay-up, ensuring no coupling between in and out-of-plane behaviour. The symmetric stacking sequence can be identified using Figure 4.1. It is expected that the non-standard metal thickness will have no influence on the final outcome. As the model is capable of predicting any type of Glare and the selected lay-up lies within the validity range of the model.

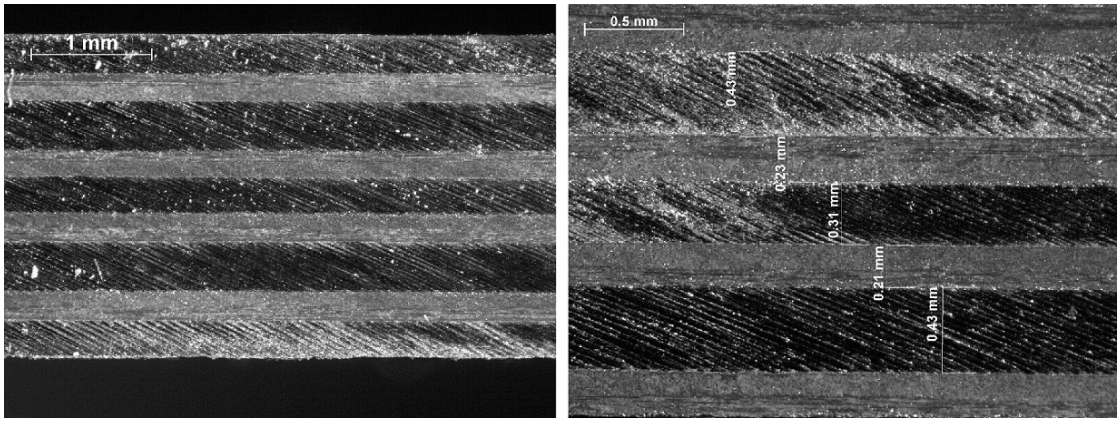

Figure 4.1: Typical cross section of Glare 3 5/4 0.3-0.4 magnified respectively, 5x (left) and 8x (right) times.

The main advantage of selecting a TU Delft stock panel is the well documented history including C-scan images, indicating the quality of the panel. The panel selected was part of a large production batch made at Fokker in 2000. Despite the well documented history, no data could be retrieved anymore. Therefore it is assumed that this panel is produced according to the standard procedures and passed all quality control checks.

4.1.2 Test sample stiffener selection

Similar to the selection of a material for the skin, a material for the stiffener is selected. The material selection for the stiffener is mainly based on practise and production aspects. As currently the application of fibre metal laminates in fuselage panels is accompanied with metal stiffeners [45, 46], it was decided to use a monolithic stiffener made of aluminium.

Subsequently, the type of alloy and thickness of the aluminium was selected based on the aluminium alloys commonly applied in the aerospace industry and availability at the TU Delft. Using these requirements aluminium 2024-T3 alloy was selected as stiffener material. This alloy is one of the most applied aluminium alloys in aircraft structural components due to the high strength and fatigue resistance [19], resulting in an ideal material for stiffeners.

Parallel to the selection of the aluminium alloy the different thicknesses available of aluminium were considered. As described in Section 2.6, the model simplifies the stiffener by assuming a rectangular equivalent stiffener. Therefore it is decided to produce an aluminium strip having a rectangular cross section matching the cross sectional area of the an actual stiffener. This way the developed panels are in close agreement with the model assumption and minimising the effect of the stiffener geometry on the actual test results. To model the effects of a stiffener accurately, an aluminium thickness was selected based on the actual flange width. This way the stiffening effect is located over the same width and is expected to behave similar as actual stiffener. Taking into account these consideration, it was chosen to use 12.5 mm thick aluminium.

Splice concept

Additional to the stiffener selection, the current trend in the design of fibre metal laminate structures is to locally add material around splices and overlapping the metal sheets. This is done to protect and stiffen the locally induced discontinuities [18, 47] and enhances the damage arrest capabilities. An example of such application is given in Figure 4.2. In this figure an extra layer of fibre material as well as an overlap of metal can be identified, increasing the thickness locally. The additional material is therefore included in the equivalent stiffener area to enhance the physical resemblance. The current trends are to apply a 100 mm wide overlap, however investigations are performed to reduce the width to 60 mm [48]. Therefore a strip of 60 mm is accounted for in the equivalent stiffener design.

4.1.3 Test sample dimensions

Using the constraints set in the previous sections for the skin and stiffener, the remainder of the dimensions can be determined. Therefore the following parameters used by Ypma are retrieved:

- skin-stiffener ratio, given by: $\left(\frac{(EA)_{sk}}{(EA)_{st}}\right)_{Ypma} = \left(\frac{(EA)_{sk}}{(EA)_{st}}\right)_{design}$
- skin width

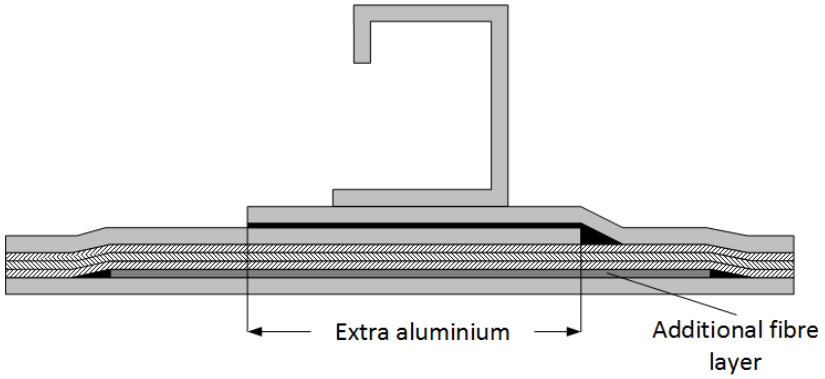

Figure 4.2: Internal splice design developed by Airbus [48].

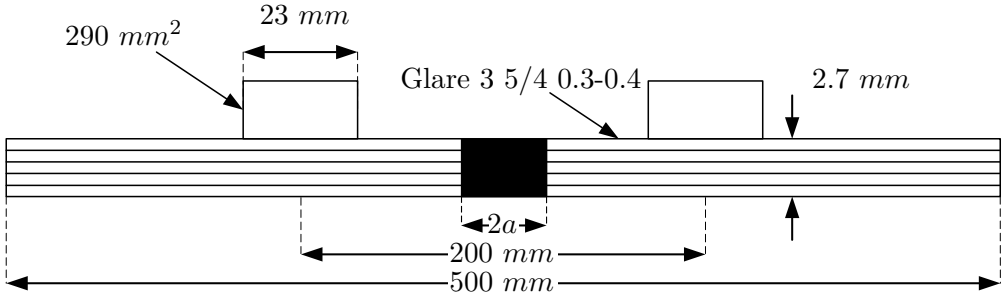

Figure 4.3: Schematic cross section of the developed stiffened panels.

This results in an sample width of 300 mm and equivalent stiffener width of 22.5 mm. Comparing this with the currently applied width in the Airbus A320 (±23.5 mm) and used during the test series of Ypma (±28 mm) a similar width is obtained [41, 46, 49].

The dimensions and materials are subsequently used as input in the model to predict the residual strength. It was observed that the limited width of the panel (300 mm) would have a large influence on the predictions. It affects the prediction in a way no crack arrest predictions could be made, due to the large effect of the finite width correction. Therefore it was decided to increase the width of the panel to 500 mm, reducing the effect of the finite width on the prediction and enabling the prediction of crack arrest. This results in a slightly modified design of the test samples, given in Figure 4.3 and B.1.

Neutral axis determination

Normally during flat panel residual strength tests, the sample is vertically displaced, while clamped on both sides. This induces in-plane deflections as the panel is loaded in the neutral line. In the development of experimental stiffened panels, the sample is no longer flat due to the presence of stiffeners on one side, which run all the way into the clamps. This requires an equally thick tap on one side, resulting in a shift of the

neutral line towards the stiffener side. However to achieve only in-plane deflections, the neutral line should be centred. Therefore the neutral axis must be determined using Equation 4.1 [38] to account for in the tap sizes.

$$\bar{y} = \frac{\sum EAy}{\sum EA} = 4\ mm \tag{4.1}$$

Where the stiffness E_{sk} and E_{st} are respectively 57.7 and 72 GPa and other parameters can be determined using Figure 4.3. As a result the neutral axis is located 4 mm above the bottom of the skin. Subsequently, it is possible to determine the size of the tap, which should be positioned on the back side of the panel. This results in a back-tap of 7.2 mm.

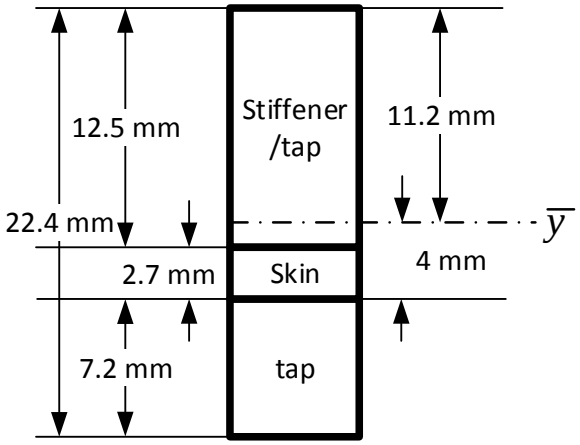

Figure 4.4: Schematic cross section of the tap configuration and dimensions.

4.2 Initial crack length determination

Parallel to the design of the samples fixed dimensions, the initial crack length is determined. With this parameter, the different stages in the residual strength diagram of a stiffened structure should be captured, indicated as; unstable crack growth without crack arrest, unstable crack growth before crack arrest and stable crack growth until failure [18, 30, 35]. These different stages can be identified in Figure 4.5 by respectively $a_{0,1,2}$. Therefore the initial crack length is varied over the four different samples, in a way that one initial crack length will result in unstable crack growth without crack arrest, two samples should indicate unstable crack growth before crack arrest and finally one initial crack length would result in stable crack growth until failure. Taking into account these considerations, the model is used to predict the initial crack lengths, resulting in the dimensions given in Table 4.1. The predicted crack growth path will subsequently be discussed in Chapter 5.

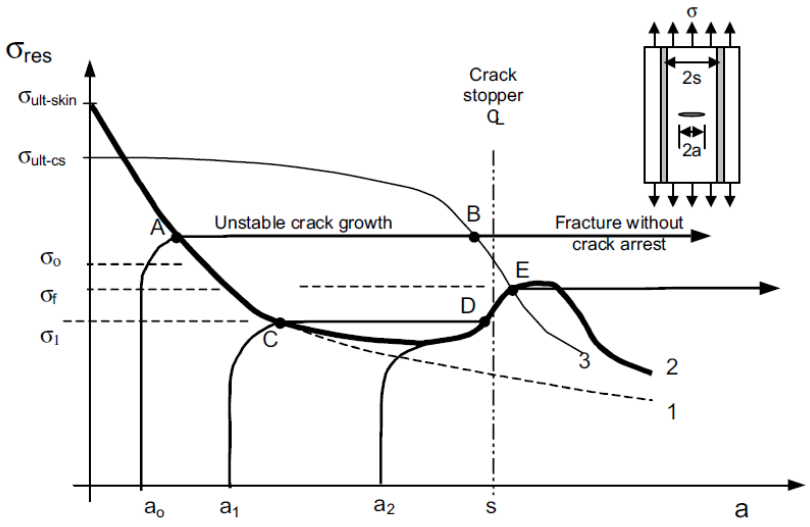

Figure 4.5: Schematic illustration of the three different stages in the residual strength diagram of a stiffened structure [18].

Table 4.1: Derived initial crack lengths based on model predictions.

	2a [mm]	2a/W [-]	reference curve in figure
Panel 1	40	0.08	a_1
Panel 2	100	0.2	a_2
Panel 3	50	0.1	a_1
Panel 4	20	0.04	a_0

4.3 Production process

The test sample design discussed in Section 4.1 is subsequently produced at the Department of Aerospace Structures and Material Laboratory (DASML) in the faculty of Aerospace Technology at the TU Delft. After acquiring the materials, all materials where cut to the desired size, followed by deburring, sanding and cleaning. After which the position of the taps and stiffeners was determined. Finally before bonding the metal components are pretreated to increase the adhesion of the epoxy adhesive as is discussed next.

4.3.1 Metal pretreatments

Similar to the pretreatment of the skin, the metal components are pretreated to guarantee a good bonding interface. The quality of this bond interface is of great importance to ensure good load transferring capabilities between the interfaces. Therefore the stiffeners are anodised and taps are etched. The anodising process results in a controlled surface roughness enhancing the adhesion, while the etching is considered to give sufficient adhesion required for the taps. This ultimately results in the preparation steps enumerated next, to achieve the required surface finish.

Stiffeners: cleaned → etched → anodised → primed

Taps: cleaned → etched

The applied procedure and function accompanied to the individual steps is subsequently discussed in Appendix B. This results in a pretreated surface similar to that currently applied in structural components of aircraft [50]. After completing the pretreatment procedure for the stiffener and taps, the bond interface can be created. Therefore the same FM 94 epoxy film is used as during production of the Glare skin [18, 51]. In preparation the film should be taken out of the freezer a day prior to production and cut in sizes equal to the bond area. Followed by cleaning of the substrates using acetone after which the film can be attached to either the taps or skin.

When all parts are bonded the sample is put in a vacuum bag to cure in an autoclave. Following the standard auto clave cycle indicated by the supplier [51], which implies heating to 121 ℃, applying a pressure of 0.28 MPa and maintaining for at least 60 minutes at 121 ℃± 3 ℃. Finally the initial crack sizes are created using a fret-saw for the small crack and jigsaw for the larger cracks.

4.4 Panel analysis

The application of an interface between the skin and the stiffener induces a possible place for defects. To be able to ensure a good interface, the bond should be analysed. Therefore it was decided to analyse the panels by means of an ultrasonic C-scan. A C-scan measures the signal loss when emitting ultrasonic waves through the material [52]. A high signal loss indicates a defect in the material, which could be for example an inclusion, delamination or dry spot. Additionally as discussed in Section 4.1.1 no data for the skin used in the test specimen was available. So by analysing the bond interface also insight in the structural health of the skin is gained. Ultimately it was obtained that both the skin and skin-stiffener interface do not possess of any defects, therefore all panels passed the quality control. The C-scan images supporting this conclusion are given in Appendix B.

Besides the C-scan analysis the test samples are measured to check the correlation between the predefined dimensions and the actual samples. Therefore the thickness, stiffener width and initial crack length are measured, which are considered to be the most important parameters. The thickness is measured using a Mitutoyo thickness gauge and the stiffener width and initial crack length using a digital jaw calliper. As a result the averaged dimensions, given in Table 4.2, are obtained, the individual results and locations are subsequently shown in Appendix B.

Table 4.2: Averaged test samples key dimensions.

	Panel 1	Panel 2	Panel 3	Panel 4
Skin thickness (t) [mm]	2.683	2.685	2.680	2.684
Stiffener width (w_{st}) [mm]	23.12	23.00	23.07	22.90
Initial crack length ($2a$) [mm]	39.33	100.00	49.90	19.14

4.5 Test set-up

Once the test samples have been finalised, the test set-up is prepared. The test samples are tested in the lab of the faculty of Aerospace Engineering. Therefore a 1000 KN MTS fatigue machine is used, consisting of hydraulic actuators. Using this machine the load is introduced onto the sample by means of clamping plates.

After the sample is installed in the test bench the additional equipment is prepared. Therefore a microscope is attached to a xyz-table to measure the crack length. The microscope is subsequently connected to a computer together with an USB webcam. This way it is possible to store both the visible crack size, applied force and test bench displacement simultaneously. The xyz-table is used to enable the measurement of both the left and right crack length by moving the table as the microscope range is limited. This is schematically illustrated in Figure 4.6, the actual test set-up is subsequently shown in Appendix B.

Additional to the equipment discussed above, is the first experiment equipped with two strain gauges and Digitial Image Correlating (DIC) equipment. The strain gauges were used to monitor the progress of the test supporting the predictions and observations. The DIC equipment was applied to validate the plastic zone correction of Irwin. It is expected that the presence of the stiffener will influence the plastic size growth. Therefore the stiffener side of the sample is painted white, with a carefully created black mesh enabling the analysis of the strain field of both the skin and stiffener. The results of this extra equipment is discussed in Chapter 5 and is highlighted with a dashed line in Figure 4.6.

The test samples are finally prepared by applying millimetre paper parallel to the crack to measure the crack length. This way the physical crack length can be measured during every load increase by means of photos taken with the microscope.

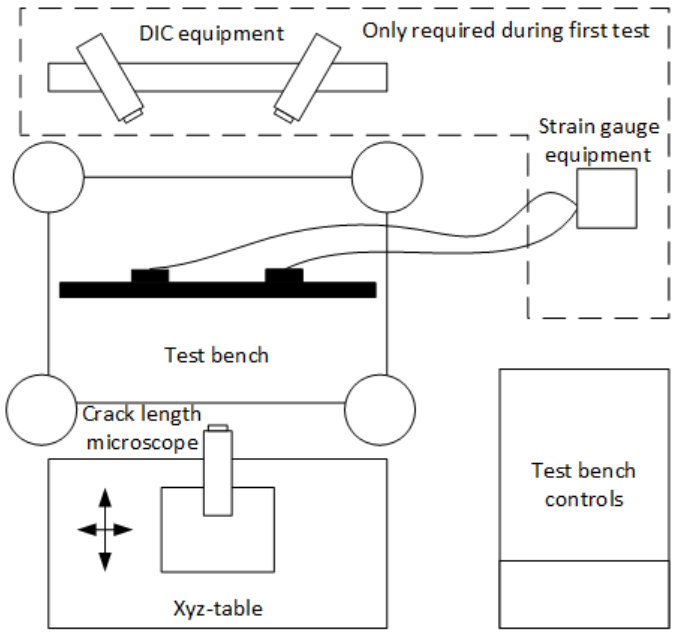

Figure 4.6: Schematic illustration of the test set-up used.

4.6 Test procedure

The tests are subsequently performed using a predefined standard procedure. In this procedure the required operations are discussed during every step. Therefore primarily the test method should be selected, which is either displacement or load controlled. During the experiments it is expected that at the onset of unstable crack growth a reduction in load is present, similarly to that of failure during flat plate residual test, before the stiffener presence will induce a load increase. This phenomena can only be captured with displacement controlled testing, enabling the monitoring of the unstable crack growth region. Therefore it was decided to perform displacement controlled experiments, which requires the definition of the amount of displacement per step.

The step size should subsequently be small enough capturing the different phases of the crack growth diagram, while maintaining a manageable data output for processing. Therefore it was decided to use a step size of 0.1 mm. Since initially a displacement of 5 mm of the test bench was approximated this would results in 50 steps. During the first test it was observed that the step size was still too large, resulting in an too abrupt load introduction. Therefore during the remainder of the test a step size of maximal 0.05 mm was taken. Additionally, the slope during every load step was defined as well, resulting in a more controlled load introduction i.e. the displacement is applied with 0.005 m/s.

After every displacement increase, a period of time is waited before measurements are taken. This has been done because an amount of relaxation in the structure is expected, which will result in an initial load overshoot before a final constant load can be obtained. Therefore the measurement is taken after waiting at least half a minute. This concludes the procedure performed during every test cycle and is summarized below.

Test summary

- Displacement controlled
- Displacement step size of 0.1 mm for first sample
- Displacement step size of max. 0.05 mm for remainder of samples
  - Displacement introduced with 0.005 mm/s
- Half a minute relaxation before measurement

Chapter 5

Test predictions, results and validation

During the final phase of the model development, a set of four test samples are designed to validate the model. These samples were required as non of the experiments obtained from literature indicate the crack arrest phenomena. Therefore tests are performed to identify crack arrest before failure, varying the initial crack length while keeping all other dimensions constant. In this chapter initially the predicted results of the experimental program are discussed based on the developed method, followed by the test results obtained.

5.1 Test predictions

Before the analysis of the crack arrest capabilities of the stiffened structures is validated, the test results are predicted. Therefore the model structure and input parameters derived in respectively Chapter 3 and 4 are used. The non standard aluminium thickness, discussed in Section 4.1.1 is subsequently averaged over all aluminium layers and other material properties are given in Appendix D. This enables the identification of the three separate phases of the crack growth diagram as discussed in Section 4.2 [18, 30] and has resulted in the initial crack lengths given in Table 4.1.

Subsequently for every sample the model computes a crack growth and stiffener failure diagram. The crack growth diagram indicates the onset of unstable crack growth, crack-arrest and final failure of the skin, while the stiffener failure diagram indicates the onset of stiffener yielding and failure (highlighted with respectively 1 and 2 in the figures). Using the output generated the crack growth characteristics can be predicted. In Figure 5.1 and 5.2 this has been done for an initial crack length of 40 mm. As can be seen in the figure it is expected that a large region of unstable crack growth is visible (horizontal part) before crack arrest will happen. Subsequently the load is increased until the load passed the maximal allowable stress of the stiffener, at this point stiffener failure will result in final failure of the panel, at a gross stress of 319 MPa.

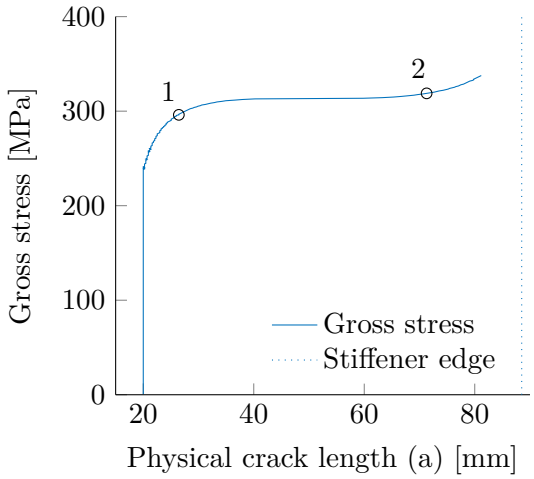

Figure 5.1: Residual strength predictions for test sample 1, $2a/W = 0.08$, $W = 500\ mm$.

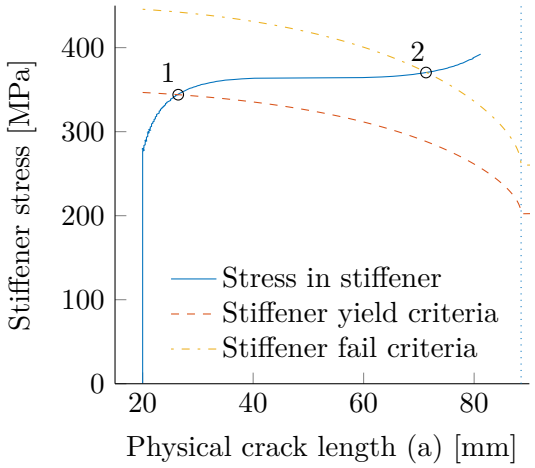

Figure 5.2: Stiffener failure determination for test sample 1, $2a/W = 0.08$, $W = 500\ mm$.

Due to importance of the identification of crack arrest in this thesis a secondary test sample has been equipped with a similar initial crack length. Therefore the sample consist of an initial crack length of 50 mm. Subsequently the crack growth characteristics are presented in Appendix D. It can be seen that due to the increase in crack length a slightly larger region of stable crack growth is expected before unstable crack growth and crack arrest will happen. This results in failure of the sample at a gross stress 316 MPa, due to stiffener failure.

After the prediction of the main objective; crack arrest, two additional samples are tested, which should indicate unstable crack growth without crack arrest and stable crack growth before failure. Therefore a sample is equipped with an initial crack length of 100 mm, as can be seen in Figure 5.3 and 5.4. Based on the figure it can be obtained that no unstable crack growth is present due to the lack of horizontal region in the applied load. Instead it is expected that the load will increase in a stable manner until failure of the stiffener, at a gross stress of 298 MPa.

Finally unstable crack growth without crack arrest is expected to happen with very small cracks, when the amount of energy released during unstable crack growth becomes too large to be arrested by the stiffener. Therefore a test sample is equipped with an initial crack length of 20 mm. Figure 5.5 and 5.6 subsequently predict the crack growth path, which consist of a small region of stable crack growth before sudden failure of the skin. The model indicates that the influence of the stiffener on small cracks is indeed marginal, resulting in unstable crack growth of the skin without crack arrest, at a gross stress of 301 MPa.

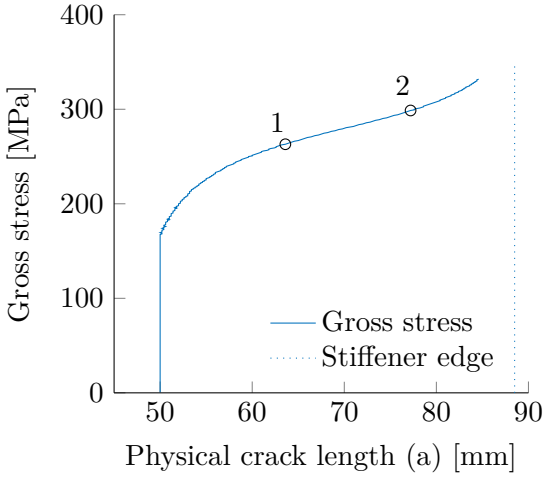

Figure 5.3: Residual strength predictions for test sample 2, $2a/W = 0.2$, $W = 500\ mm$.

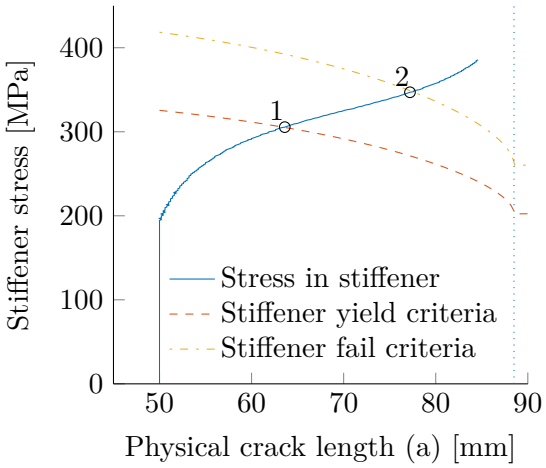

Figure 5.4: Stiffener failure determination for test sample 2, $2a/W = 0.2$, $W = 500\ mm$.

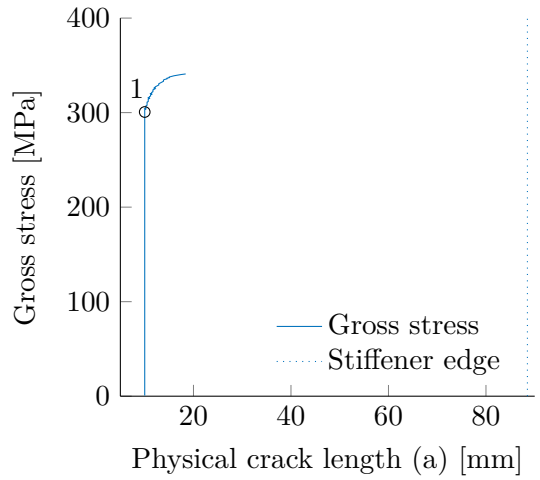

Figure 5.5: Residual strength predictions for test sample 4, $2a/W = 0.04$, $W = 500\ mm$.

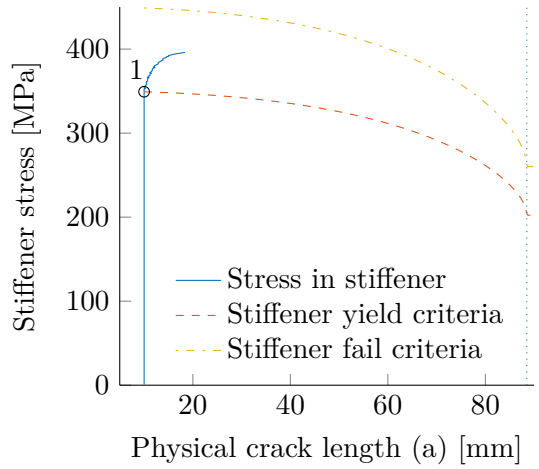

Figure 5.6: Stiffener failure determination for test sample 4, $2a/W = 0.04$, $W = 500\ mm$.

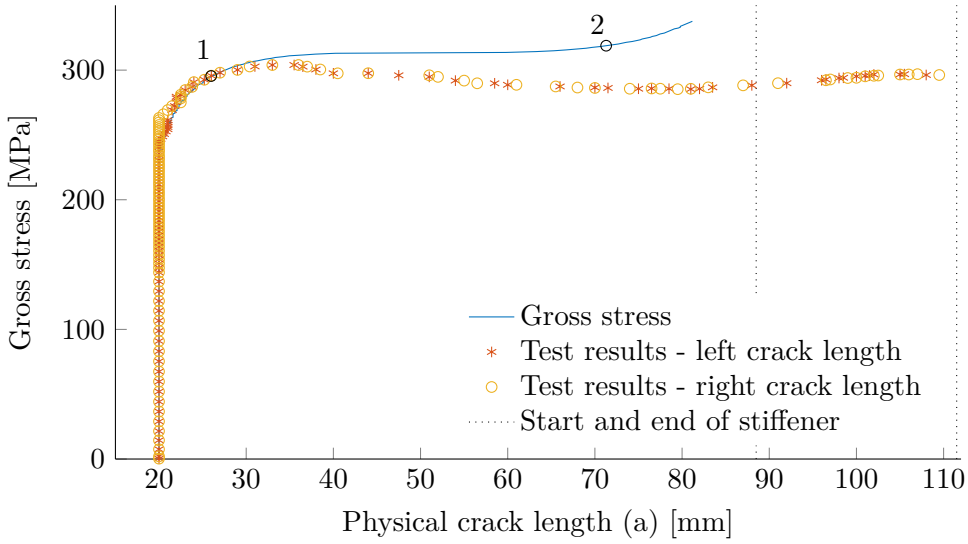

Figure 5.7: Test result comparison with prediction for test sample 1, $2a/W = 0.08$, $W = 500\ mm$.

5.2 Test results and validation

The test predictions are subsequently compared with experimental data from the experiments. Therefore the tests are executed as discussed in Section 4.6, resulting in Figure 5.7, 5.9, 5.8 and 5.10. In this section subsequently the comparison between the test predictions and results is made. The test results consists of both the left and right crack length measurement, indicated in the figures.

Figure 5.7 illustrates the comparison between the test results and prediction for an initial crack length of 40 mm. The model prediction follows the trend of the experimented well until the initiation of unstable crack growth, at ± 35 mm. Here the model predicts a constant stress until close the stiffener, while in practise a load reduction can be obtained. The onset of this difference is initiated at stiffener yielding, highlighted at one. Finally a load increase is observed below the stiffener before final failure of the sample, due to unstable crack growth of the skin.

A similar observation can be done for the test sample containing an initial crack of 50 mm, as given in Figure 5.8. Again the prediction correlates rather well until the crack becomes unstable, at ± 40 mm. At this point a load reduction is observed before crack-arrest and final failure is induced. The sample finally failed due to unstable crack growth of the skin when the crack passed the stiffener.

After the assessment of the crack arrest samples, the remainder of the samples were tested, to identify the different crack growth stages, as discussed by Vlieger [30]. In Figure 5.9 therefore stable crack growth until failure was predicted for an initial crack length of 100 mm. As can be seen in the figure indeed only stable crack growth is observed during the test. Despite the identification of stable crack growth, the method predicts a too small crack initiation stress. Therefore the prediction results in a very conservative crack growth path while in practise the crack initiates about 50 MPa higher. Again final failure was induced due to unstable crack growth of the skin.

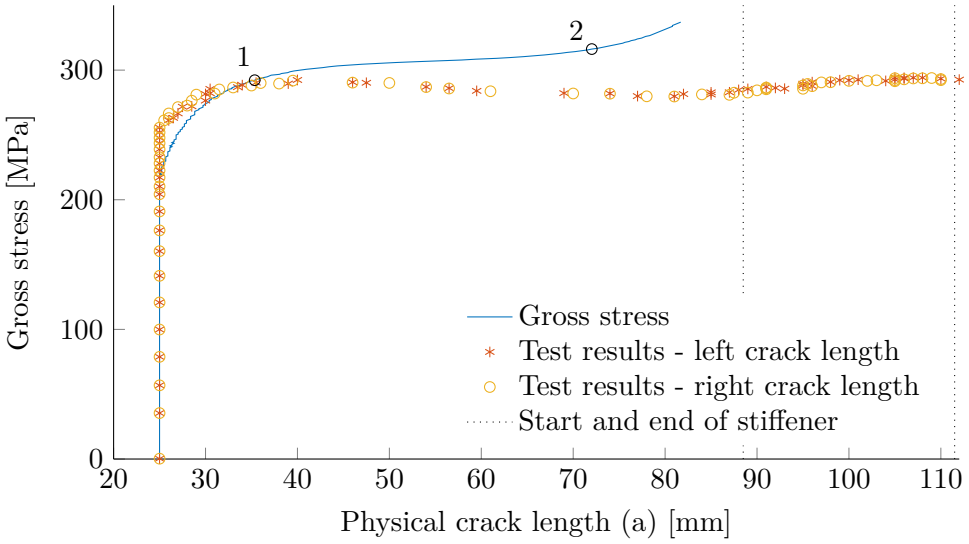

Figure 5.8: Test result comparison with prediction for test sample 3, $2a/W = 0.1$, $W = 500\ mm$.

The last sample is subsequently equipped with an initial crack length of 20 mm to indicate unstable crack growth without crack arrest. Therefore a small crack length is chosen, minimising the stiffener influence. Subsequently Figure 5.10 presents the comparison between prediction and test results. A good correlation is obtained in the prediction of the residual strength, only a slightly higher stress is predicted after the initiation of stiffener yielding. Subsequently the test again indicates a load reduction until the stiffener is reached. At this point unstable crack growth was observed, resulting in final failure of the panel.

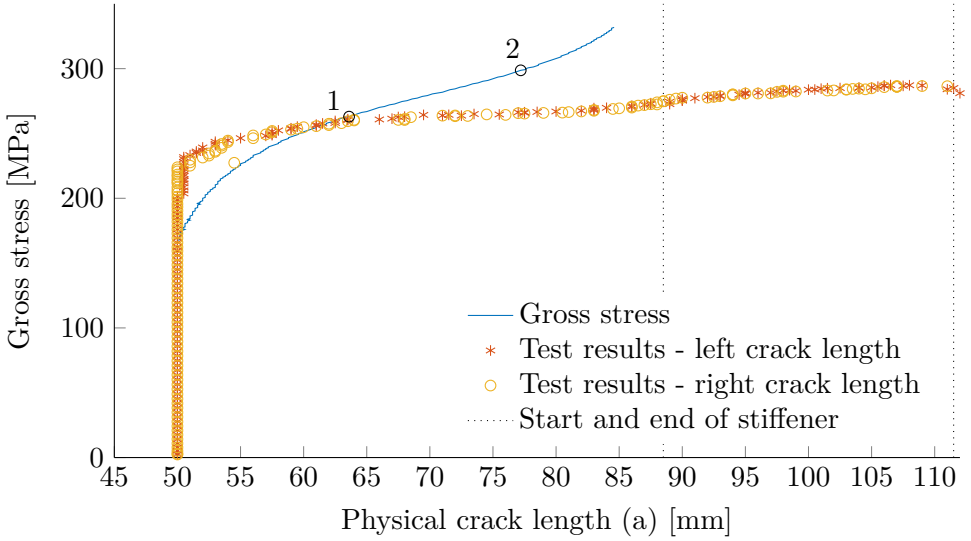

Figure 5.9: Test result comparison with prediction for test sample 2, $2a/W = 0.2$, $W = 500\ mm$.

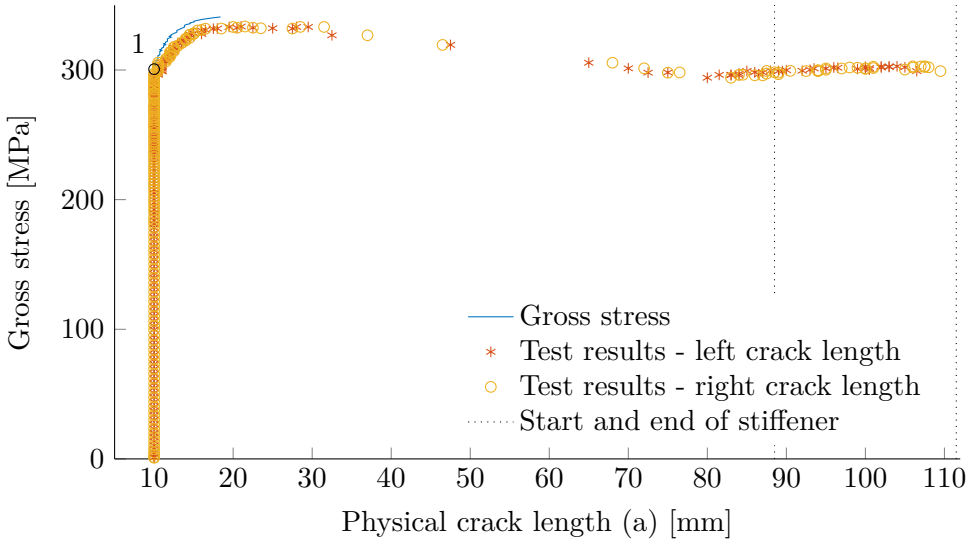

Figure 5.10: Test result comparison with prediction for test sample 4, $2a/W = 0.04$, $W = 500\ mm$.

5.3 Digital image correlation results

In Chapter 4 the application of Digital Image Correlation (DIC) on one of the test samples has been discussed, to observe the effect of the stiffener on the plastic zone size. The model assumes that the Irwin plasticity correction can be used [27], without taking into account the lateral resistance of the stiffener. However it is expected that the presence of the stiffener will affect the plastic zone. Therefore DIC equipment is used.

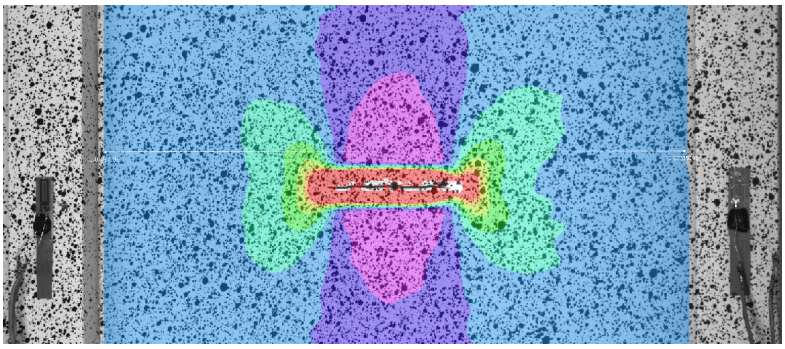

Figure 5.11: Strain field during the first phase of the crack growth path of test sample 1.

In Figure 5.11 subsequently an arbitrarily moment is taken during the first phase of the crack growth path. In this first phase the crack is relatively small and the stiffener influence is expected to be marginal. As can be seen in the figure indeed the typical butterfly shape is present supporting the observation of a small influence of the stiffener. When the crack starts extending, illustrated by Figure 5.12. It can been seen that the shape has become different, instead of a butterfly shape, a more circular shape can be identified. Additional the observation can be made that the plastic zone stops expanding and only moves along with the crack-tip.

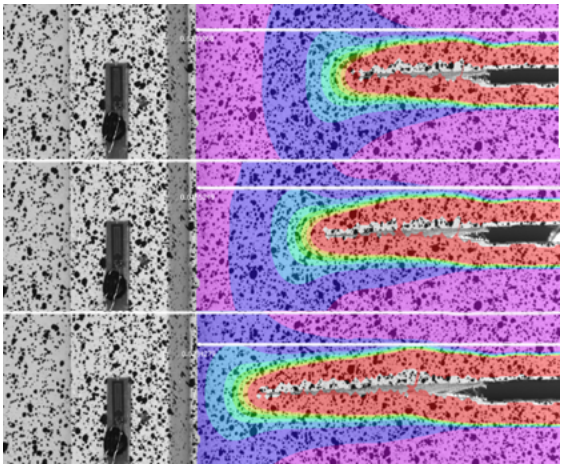

Figure 5.12: Three stages of the crack growth path with a similar strain field for test sample 1 (approximate 25 mm crack growth).

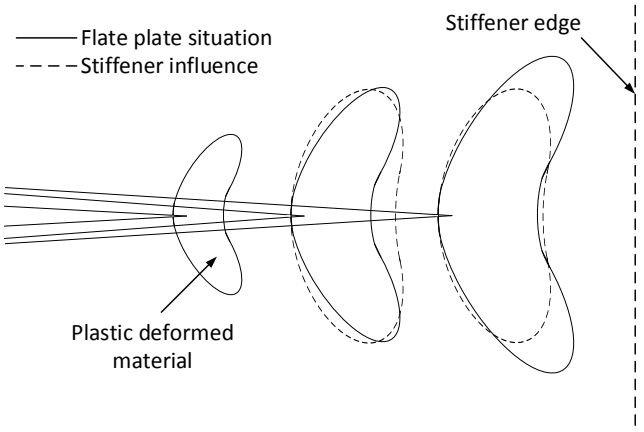

Figure 5.13: Schematic illustration of stiffener effect on plastic zone growth.

Based on these observations it can be concluded that the plastic zone is affected by the stiffener. At a certain point during the test the plastic zone shape transforms from a typical butterfly to a more circular shape, caused by the stiffener presence. After this transformation it can also be observed that the plastic zone does not increase in size anymore. This process has been schematically illustrated in Figure 5.13. As result a different plastic zone can be expected with respect to a flat plate and is further discussed in Chapter 6.

5.4 Conclusions

The results achieved with the prediction method correlate well with the experimental data for small crack lengths while for a large crack length a mismatch in crack initiation can be identified. Table 5.1, subsequently shows that the prediction of the failure stresses are close to the stresses observed during the experiments. However, it can also be observed that three out of four failure modes where predicted incorrect. Therefore an extra verification step should be performed, analysing the difference in failure mode. This is further discussed in Chapter 6.

Table 5.1: Failure mode and residual strength comparison between predictions and experimental test results.

	Predicted failure mode	Predicted failure stress [Mpa]	Actual failure mode	Actual failure stress [Mpa]	Difference [%]
Panel 1	Stiffener failure	319	Skin failure	304	104.9
Panel 2	Stiffener failure	298	Skin failure	297	100.3
Panel 3	Stiffener failure	316	Skin failure	294	107.5
Panel 4	Skin failure	341	Skin failure	333	102.4

Chapter 6

Discussion and verification

The experimental validation has revealed a difference between the developed model and practise. In this chapter the inequalities observed are discussed and verified with the characteristics of the model. It was observed that for small cracks the inequality can be appointed to the introduction of yielding, affecting the crack growth characteristics while for large cracks the plastic zone correction is inadequate in prediction the effective crack length. The discussion is subsequently finalized with the differences caused by the experimental procedure performed.

6.1 Linear-elastic assumption

The first factor causing a mismatch in the crack growth path, can be attributed to the assumption of a linear-elastic stiffener. The model assumes all materials to behave linear-elastic until failure, while accounting for plasticity ahead of the crack-tip. This implies the simulation of an elastic stiffener until failure, however in practise the elasticity modulus will decrease when the yield strength of the material is exceeded. This effect has not been taken into account in the model and results in an overestimation of the load-carrying capabilities of the stiffener.

Following this observation the effect of the reducing elasticity modulus on the crack growth predictions is analysed. It is expected that due to stiffener yielding the stiffener becomes less effective, reducing the SIRF and SLCF. Therefore the model has been used to indicate the impact of the elasticity modulus of the stiffener. As result it was obtained that the SLCF initially increases before decreasing with respect to the original elasticity modulus of 72 GPa, this indicates an optimum. Therefore the elasticity modulus is varied as function of the SLCF at a specific location, in this case the stiffener edge [1] (illustrated in Figure 6.1). It can be seen that for a low elasticity modulus the SLCF is close to zero indicating an ineffective stiffener, while for a large stiffener-elasticity-modulus (> 1000

[1] Note in this discussion the analysis is performed at the stiffener edge while any point can be taken. However it is expected that at the stiffener edge the effect is the most dominant, due to the same location of the crack-tip and stiffener edge

GPa) the curve will eventually become one, indicating that the stiffener attracts all loads.

Considering the applied test case with a stiffener-elasticity-modulus of 72 GPa it can be observed that the SLCF initially will increase while the load carrying capabilities will reduce. This effect is expected to be present until the peak of the SLCF curve (Figure 6.1) at 20 GPa, which relates to a stress of 380 MPa, using the Ramberg-Osgood relation [26]. Therefore it is not possible to predict the stress difference based on the SLCF as the effect of both the decrease in elasticity modulus and increase in SLCF cannot be adequately assessed together. Additionally the stiffener load concentration factor is only assessed directly ahead of the crack-tip, while at the onset of plasticity, energy is dissipated away in irreversible deformation of the material. This effect complicates the process even more and is not captured by the model.

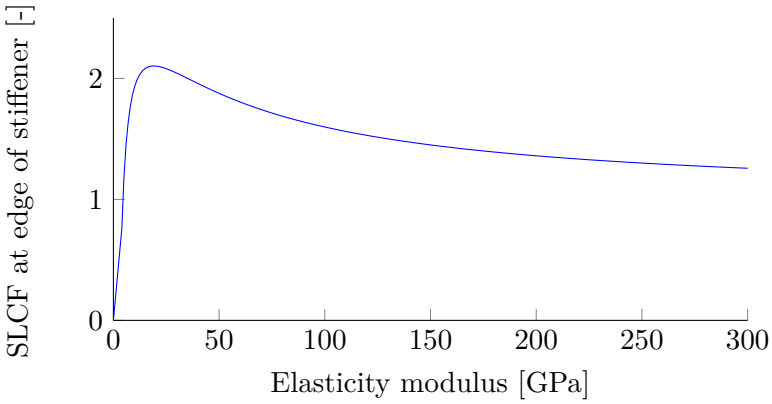

Figure 6.1: Stiffener-elasticity-modulus influence on the SLCF.

Besides the SLCF, the SIRF can be analysed. This parameter indicates the stress intensity reduction and is expected to be less effective as the elasticity modulus of the stiffener will decrease. As result the skin will be more prone to unstable crack growth, supporting the fracture process observed during the tests. Figure 6.2 illustrates the effect of the elasticity modulus on the SIRF at the stiffener edge. At a low elasticity modulus, the stress intensity factor of the stiffened structure is equal to the stress intensity factor of a flat plate. Increasing the elasticity modulus will eventually result in again a SIRF of one. Subsequently, as illustrated in the figure, indeed a less effective SIRF can be obtained, when considering the applied case of 72 GPa. This results in a higher stress intensity factor in the skin when the stiffener starts yielding and supporting the observations of unstable crack growth instead of stiffener failure.

The effect of the reduced elasticity modulus is subsequently implemented in the model. Ideally the model structure should be modified accounting for the decrease in stiffener modulus, when the yield stress has been reached. This would result in a new computation of the SIRF and SLCF, for every new load and crack increase and requires an iterative procedure, which is not included in the current model. Therefore the elasticity modulus is assumed to be lower during the entire prediction. As result it is expected that the predicted stress will decrease and results in a lower skin failure stress. Figure 6.3 subsequently presents the results of this simulation for test sample 3, including the onset

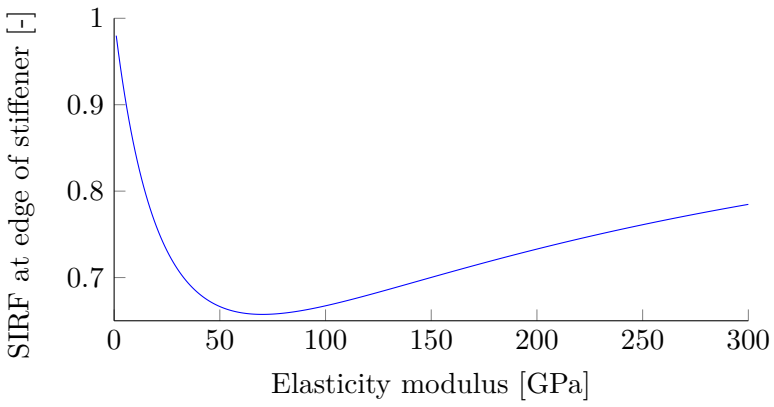

Figure 6.2: Stiffener elasticity modulus influence on the SIRF.

of stiffener yielding for stiffener modulus of 72 GPa (highlighted with number 1). It can be seen that the predicted stress indeed is reduced due to the lower elasticity modulus and failure is more likely to be caused by unstable crack growth. This is clearly illustrated in the figure at a stiffener-elasticity-modulus of 5 GPa, here the method predicts a lower critical stress and crack length.

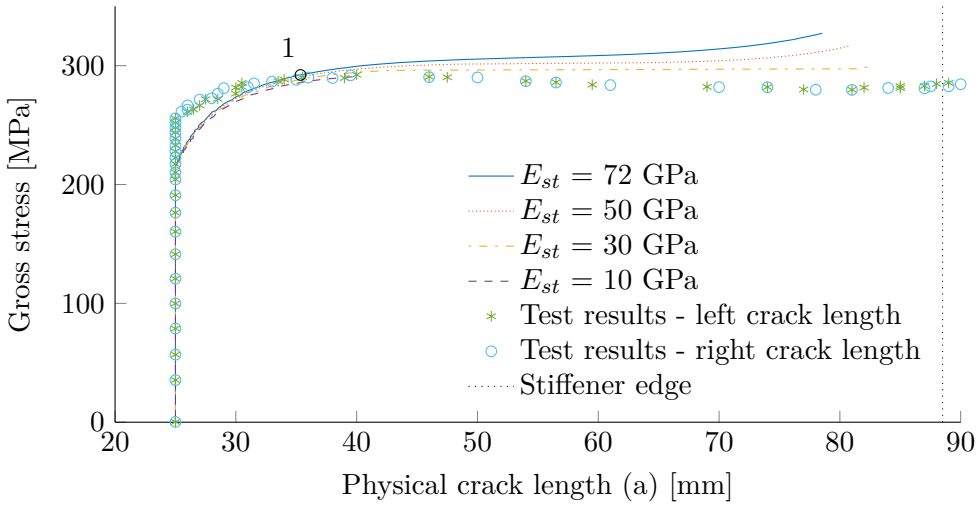

Figure 6.3: Effect of different elasticity moduli on crack growth prediction.

6.2 Effective crack length determination

The second observation done during the tests, is a mismatch in crack initiation stress between the prediction and test results for larger crack sizes. In Chapter 4, one experiment has been discussed, consisting of a initial crack length of 100 mm (test sample 2). Based on the experimental data it can be seen that the model predicts a lower initiation stress, resulting in a different crack path. This difference in crack initiation stress is expected to be caused by the deformation constraint induced by the stiffener.

In the prediction of the effective crack length, the Irwin plasticity correction assumes a linear-elastic material. This way a plastic zone size is predicted without taking into account the deformation constraint set by the stiffener. As a result of the simplification an overestimation of the effective crack length and subsequently the crack initiation stress can be expected. This observation is subsequently supported by the analysis performed in Section 5.3 indicating an altered plastic zone due to the stiffener presence.

A second explanation for the difference in the crack initiation stress could be appointed to the limitation of the Irwin plasticity correction method. As discussed in Section 3.5.2, the Irwin method [27] predicts an effective crack length growth immediately after load introduction, while in practise the effective crack length growth is initiated close to the crack initiation stress. This observation results in a different crack length prediction during the initiation phase [18]. However considering the flat plate verification, given in Section 3.5.2, it can be seen that the predictions are close to the test results, with a similar 2a/W ratio. Therefore it can be concluded that the limitation of the Irwin method does not contribute to the large difference induced in stiffened structures and should be associated to the stiffener presence.

Table 6.1: Influence of stiffener on the SIRF and the SLCF at the specific locations.

Initial crack length	50 mm	100 mm
SIRF	1	0.9571
SLCF	1.015	1.075

It is therefore expected that the difference in crack growth path can be appointed to the deformation constraint set by the stiffener. Following this thought the question is, when the plastic zone growth is affected by the stiffener presence. Therefore the experimental test results discussed in Chapter 5 are consulted. It can be seen that for all cases the crack initiation is predicted before actual crack initiation, except for the initial crack size of 20 mm (test sample 4). In this case the stiffener already starts yielding before crack initiation. Excluding this test, crack initiation could be affected by stiffener presence, where for an initial crack length of 100 mm the largest contribution can be identified.

Translating the stiffener influence into the parameters introduced in this thesis, the values given in Table 6.1 can be obtained, which represent the SIRF and SLCF at the location of the initial crack length. As can be seen in the table for an initial crack length of 50 mm the values are hardly affected by the stiffener resulting in a close correlation with the actual test. For an initial crack length of 100 mm both constants become affected but remain close to their original value.

Therefore the onset of the stiffener influence on the plastic zone is difficult to capture with the introduced parameters. As a result the effect of the stiffener on the plastic zone cannot be predicted accurately for an initial crack length of 100 mm. Instead a different plasticity correction should be considered when a large stiffener influence is expected.

6.3 Influence of the experimental procedure on the test results

The last aspect, not yet discussed, is the effect of the experimental procedure on the experimental results. During the production process all parts are thoroughly inspected and analysed by means of a C-scan. Therefore it is assumed that the effect of production defects can be excluded. Subsequently the dimensions of all test samples were measured, verifying the model input. It was observed that the measured data was similar to those used in the prediction method and therefore expecting to have no or a very small influence on the result.

The final aspect possibly affecting the experimental results negatively, is during the actual test itself. In Appendix C, the observations done during testing are discussed. It can be observed that during the tests, large out-of-plane deformations are present. These out-of-plane deformations are normally cancelled during a flat plate test, by applying anti-buckling guides. However for the test samples developed, the presence of the stiffener disables the application of anti-buckling guides. Therefore the crack flanks can deform freely as illustrated in Figure D.3. This results in a larger stress intensity factor, as discussed in Section 2.8 and a lower stress obtained during testing. This lower stress caused by the out-of-plane deformations is therefore expected to have a negative effect on the experimental results, resulting in a lower residual strength compared to the predictions.

Chapter 7

Conclusions and recommendations

The introduction of local reinforcements in fibre metal laminate structures has resulted in improved residual strength characteristics. As a result unstable crack growth is arrested by the presence of a stiffener. This has been successfully implemented in the model by simplifying the stiffener to an equivalent rectangular stiffener. The result enables the residual strength prediction of symmetric structures containing a stiffener in front of the crack, assuming linear elastic fracture mechanics and isostrain conditions.

Based on the model verification it can be concluded that the prediction method is able to predict the crack growth characteristics accurately. However during non of these experiments crack arrest was observed, requiring the execution of additional tests. The experimental data subsequently obtained, indicates that the prediction method is able to predict the crack growth characteristics for small to moderate cracks as long as the stiffener remains elastic. In this region the test results reveal a good correlation with the prediction method. For large cracks, crack initiation was predicted incorrectly resulting in a conservative prediction. Finally considering the assumption of an effective stiffener width, it is concluded that the crack growth path is predicted conservatively, below the stiffener.

The error observed between the experimental test results and prediction method, can subsequently be appointed to two different phenomena. The first effect identified is the stiffener plasticity influence. The current simplification of a stiffener being elastic until failure, affects the residual strength predictions incorrectly. The comparison between test results and model prediction revealed an error in the crack growth prediction at the onset of stiffener plasticising. It can be concluded that the reducing elasticity modulus on the crack growth characteristics is too large to neglect and results in an altered crack growth path. The second effect observed, was the stiffener influence on the Irwin plastic zone correction. The assumption of accounting for the stiffener by means of the stress intensity reduction factor is unable to incorporate the deformation constraint set by the stiffener as well as shape transformation. Therefore the plastic zone size is predicted incorrect, resulting in a lower crack initiation stress.

Although some mismatches are observed during the comparison, the model is able to describe the fracturing process accurately. The residual strength predictions are within

7.5 % of the actual values obtained during testing and follow mostly the same crack growth trend. Despite these results, the significant residual strength increase identified by the model has not been observed during the tests. Instead a load reduction was obtained at the onset of unstable crack growth, before the crack was arrested and again a load increase could be identified. The samples ultimately failed at a load similar to the onset of unstable crack growth (± 2%). It can be concluded that crack arrest was obtained, however some phenomena intentionally neglected have a bigger impact then expected, resulting in smaller arresting capabilities of the structure.

Recommendations

The discussion provided in Chapter 6 presents sufficient leads to improve the model. However it is emphasized that the simplified engineering philosophy of the model should be maintained, as it is a key part of this thesis. Therefore recommendations related to the model are done keeping the simple structure of the model in mind.

Following this philosophy, the first modification recommended to the model is the incorporation of stiffener yielding. Currently the model assumes an elastic stiffener until failure, while in practise the stiffener will start yielding far below the failure stress. Resulting in a model not only overestimating the capabilities of the stiffener but also the assessment of stiffener failure. As both features are affected by the decreasing elasticity modulus, it is recommended to include the reducing elasticity modulus after yielding in the model, as for example described by the Ramberg-Osgood relation [26]. This is expected to reduce the stiffener effectiveness after yielding, resulting in a structure more prone to unstable crack growth as well as a delay of stiffener failure. The benefit of this solution is maintaining the linear elastic assumption without the need of incorporating a different elastic-plastic approach. As a consequence the stress intensity reduction and stiffener load concentration factor are affected by the reduced stiffener modulus, requiring a feedback loop in the model, as illustrated in Figure 7.1.

Besides the incorporation of stiffener yielding in the model, the plasticity correction should account for the deformation constraint by the stiffener. The current method assumes the plastic zone to be equal to that of a flat plate, including the stress intensity reduction factor. However it was observed that this solution is unable to predict the plastic accurately. Instead the deformation constraint should be incorporated in the Irwin plasticity method, by means of a different correction factor or reconsidering the effective crack length method.

A possible method replacing the Irwin plasticity correction could be the strip-yield model. This method approximates the elastic-plastic behaviour by superimposing two elastic solutions, accounting for both crack opening and closing contributions [13]. This method is already successfully implemented in the residual strength prediction method of Rodi [53].

The recommendations are finalised with a modification for future testing. During the experiments out-of-plane deflections of the crack flanks were identified. As discussed in Chapter 6 it is expected that these deformations increase the stress intensity factor, which has not been taken into account in the model. Normally these deflections are cancelled during test by applying anti-buckling guides. However both the presence of

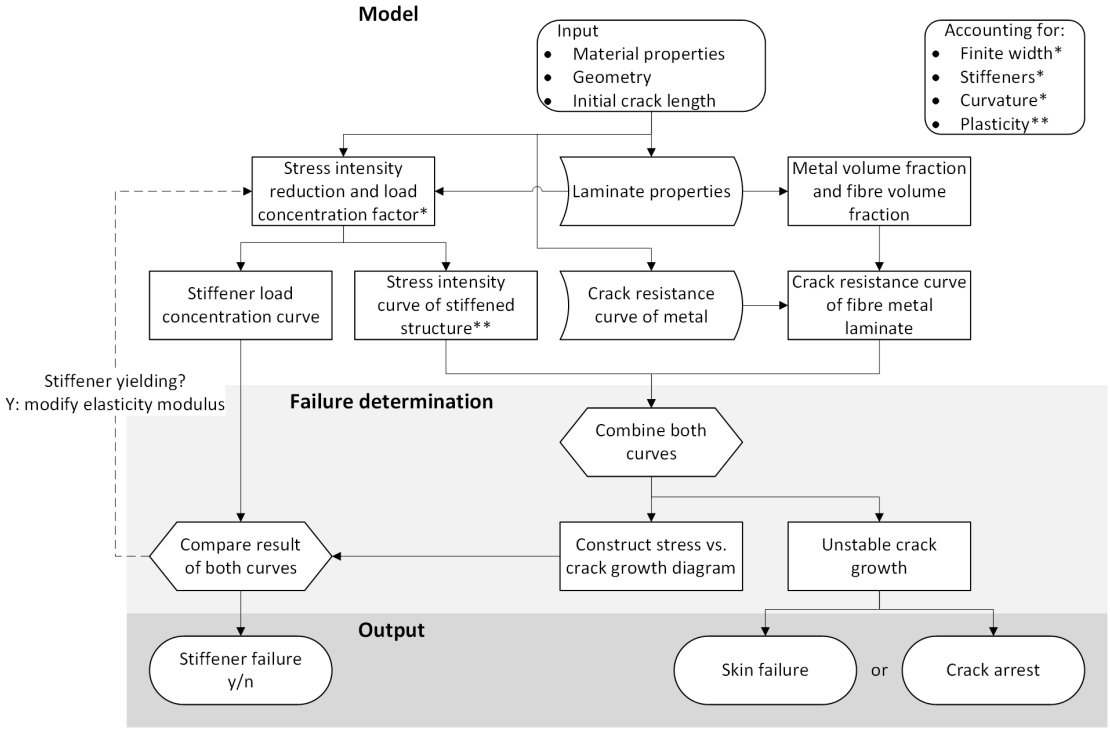

Figure 7.1: Stiffener plasticising modification to prediction method.

stiffener and panel dimensions disabled the use of anti-buckling guides. Therefore in future tests it is recommended to develop anti-buckling guides able to counteract the out-of-plane deformations and resulting in a better correlation between test and model results.

References

[1] Electronic Code of Federal Regulations. Technical report, Federal Aviation Adiminstration (FAA), 2014.

[2] L. B. Vogelesang and A. Vlot. Development of fibre metal laminates for advanced aerospace structures. *Journal of Materials Processing Technology*, 103(1):1–5, 2000.

[3] J. Pora and J. Hinrichsen. Material and technology developmetns for the Airbus A380. In *Proceedings of the 22nd International SAMPE Europe Conference of the society for the Advancement of Materials and Process Enginerring*, Paris, 2001.

[4] A. A. Griffith. The Phenomena of Rupture and Flow in Solids. *Philosophical Transactions of the Royal Society of London. Series A, Containing Papers of a Mathematical or Physical Character*, 221(582-593):163–198, 1921.

[5] H. M. Westergaard. Bearing pressures and cracks. *Journal of Applied Mechanics*, 61:A49–A53, 1939.

[6] C. E. Inglis. Stresses in a Plate due to the Presence of Cracks and Sharp Corners. (55):219–241, January 1913.

[7] C. Rans, R. Rodi, and R. C. Alderliesten. Analytical prediction of Mode I stress intensity factors for cracked panels containing bonded stiffeners. *Engineering Fracture Mechanics*, 97(0):12–29, 2013.

[8] D. Chen. *Bulging of Fatigue Cracks in a Pressurized Aircraft Fuselage*. PhD thesis, TU Delft, 1990.

[9] T. Swift. Design of Redundant Structures. *Fract Mechanics Design Methodology*, (97):9. 1–9. 23, 1979.

[10] M. F. J. Koolloos, F. P. H. Grooteman, and J. Ten Hoeve. Analysis of Residual Strength of Flat and Curved Panels, With and Without Stiffeners, With Mulitple-Site Damage. Technical report, National Aerospace Laboratory NLR, 2006.

[11] J. R. Dixon. Stress distribution around a central crack in a plate loaded in tension: effect on finite width of plate. *Royal aeronautical society*, 64:141, 1960.

[12] E. C. Feddersen. Evaluation and Prediction of the Residual Strength of Center Crack Tension Panels. *ASTM STP 486*, pages 50–78, 1971.

[13] T. L. Anderson. *Fracture Mechanics: Fundamentals and Applications, Third Edition*. Taylor & Francis, 2005.

[14] B. McGinty. Fracture Mechanics, 2014.

[15] H. Tada, P. C. Paris, and G. R. Irwin. *The stress analysis of cracks handbook: by Hiroshi Tada, with the cooperation of Paul C. Paris and George R. Irwin*. Paris Productions & (Del Research Corp.), 1985.

[16] G. R. Irwin. Analysis of stresses and strains near the end of a crack traversing a plate. *Journal of Applied Mechanics*, 24:361–364, 1957.

[17] J. Schijve. *Fatigue of Structures and Materials*. Springer, 2008.

[18] T.J. De Vries. *Blunt and sharp notch behaviour of Glare laminates*. PhD thesis, TU Delft, April 2001.

[19] C. A. J. R. Vermeeren. *The Residual Strength of Fiber Metal Laminates*. PhD thesis, TU Delft, 1995.

[20] G. C. Sih, P. C. Paris, and G. R. Irwin. On cracks in rectilinearly anisotropic bodies. *International Journal of Fracture Mechanics*, 1(3):189–203, 1965.

[21] J. M. Krafft, A. M. Sullivan, and R. W. Boyle. Effect of Dimensions on Fact Fracture Instability of Notched Sheets. In *Proceedings of the Crack Propagation Symposium Cranfield, The College of Aeronautics*, pages 8–28, cranfield, England, 1962.

[22] K. J. J. M. Zaal. *Residual strength analysis of structures in aluminium alloy and fibre metal laminates*. PhD thesis, November 1995.

[23] M. S. Ypma. Verification of the calculation method for residual strength method of unstiffened Glare panels. B2V-02-51 (restricted). Technical report, Delft University of Technology, 2002.

[24] T.J. De Vries. Plane stress fracture toughness test results of 2024-T3 clad sheet, 2024-T351 and 7475-T7351 plate aluminium alloys B2V-96094 (restricted). Technical report, Delft University of Technology, 1996.

[25] L. Schwarmann. Letter from Dr. Schwarmann (Deutsche Airbus to Dr. Roebroeks (SLC and Mr. Vermeeren. Technical report, Structural Laminates Company, 1991.

[26] N. Perez. *Fracture Mechanics*. Springer Science & Business Media, 2004.

[27] *Plastic Zone Near a Crack and Fracture Toughness*, 1961.

[28] R. Rodi, R. C. Alderliesten, and R. Benedictus. Crack-tip behavior in fiber/metal laminates by means of digital-image correlation. *Journal of Aircraft*, 47(5):1636–1646, 2010.

[29] ASTM International. ASTM Standard E561 - Standard Test Method for K-R Curve Determination, 2014.

[30] H. Vlieger. The residual strength characteristics of stiffened panels containing fatigue cracks. *Engineering Fracture Mechanics*, 5(2):447–477, 1973.

[31] J. Schijve. Crack stoppers and arall laminates. *Engineering Fracture Mechanics*, 37(2):405–421, 1990.

[32] B. G. Nesterenko. Residual Strength Analysis if Stiffened Panels using R-Curves of Skin Material. In *International Congress of the Aeronautical Sciences*, Moscow, 2004.

[33] B. G. Nesterenko. Analytically - Experimental Study of Damage Tolerance of Aircraft Structures. In *International Congress of the Aeronautical Sciences*, pages 333.1–11, Moscow, 2002.

[34] J. Schijve. *Fatigue of Structures and Materials*. Springer Science & Business Media, 2008.

[35] Afgrow. Handbook for Damage Tolerant Design. Technical report, LexTech Inc., 2014.

[36] M. Isida. On the determination of stress intensity factors for some common structural problems. *Engineering Fracture Mechanics*, 2(1):61–79, 1970.

[37] D. Broek. *Elementary engineering fracture mechanics*. Springer Science & Business Media, 1982.

[38] C. Kassapoglou. *Design and Analysis of Composite Structures: With Applications to Aerospace Structures*. John Wiley & Sons, 2nd editio edition, 2013.

[39] T. J. De Vries and C. A. J. R. Vermeeren. Memorandum M-705. Technical report, TU Delft, 1994.

[40] T.J. De Vries. Residual strength of flat Glare panels B2V-00-15 (restricted). Technical report, 2000.

[41] M. S. Ypma. Test results of residual strength test of stiffened glare panels. B2V-00-16 (restricted). Technical report, Delft University of Technology, 2003.

[42] M. S. Ypma. Manual PCRACKS B2V-98-17 (restricted). Technical report, Delft University of Technology, 2000.

[43] M. S. Ypma. Residual strength calculations using PCRACKS and experiments. B2V-00-17 (restricted). Technical report, Delft University of Technology, 2000.

[44] E. Van Hummel. Literature study - A simplified method for the determination of damage arrest capabilities in stiffened structures. Technical report, 2015.

[45] T. Sinmazçelik, E. Avcu, M. Ö. Bora, and O. Çoban. A review: Fibre metal laminates, background, bonding types and applied test methods. *Materials & Design*, 32(7):3671–3685, 2011.

[46] Airbus. Observations and measurements performed on an Airbus A380 fuselage panel, 2015.

[47] P.L. Kuijpers. The influence of single spliced layers, combined with bonded doublers, and the influence of delamination bands on the residual strength of Glare 3 material. Technical report, TU Delft, 1996.

[48] R.C. Alderliesten, C. Rans, T. Beumler, and R. Benedictus. Thin-walled hybrid structures for damage tolerant aircraft fuselages, 2003.

[49] D. Grandsen. Data Airbus A320, 2015.

[50] O. Lunder. *Chromate-free pre-treatment of aluminium for adhesive bonding.* PhD thesis, Norwegian University of Science and Technology, 2003.

[51] Cytec. FM 94 adhesive film. Technical report, 2010.

[52] J. Summerscales. *Non-Destructive Testing of Fibre-Reinforced Plastics Composites, Volume 2.* Springer Science & Business Media, 1990.

[53] R. Rodi. *The Residual Strength Failure Sequence in Fibre Metal Laminates.* PhD thesis, TU Delft, 2012.

[54] ASTM International. ASTM Standard D3933 - Standard Guide for Preparation of Aluminum Surfaces for Structural Adhesives Bonding (Phosphoric Acid Anodizing), 2010.

[55] Cytec. BR 127 corrosion inhibiting primer. Technical report, 2010.

Appendix A

Curve fits for crack resistance curve prediction method

This appendix contains the different curve fits obtained by De Vries and Ypma in the development of the crack resistance method for fibre metal laminates. Therefore two different sets of curve fits are determined for respectively loading and transverse direction.

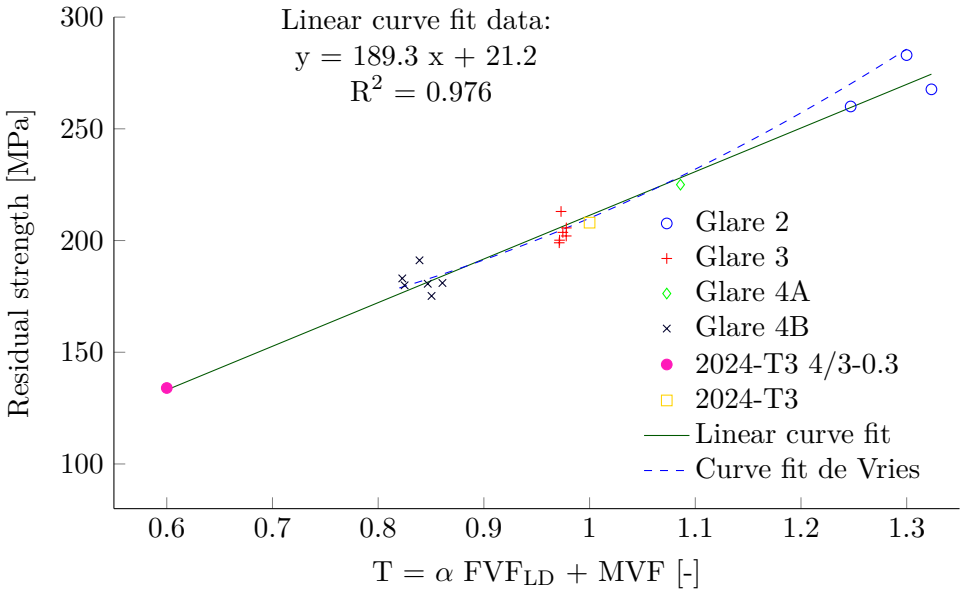

Figure A.1: Residual strength as function of T in L-T direction [18, 23].

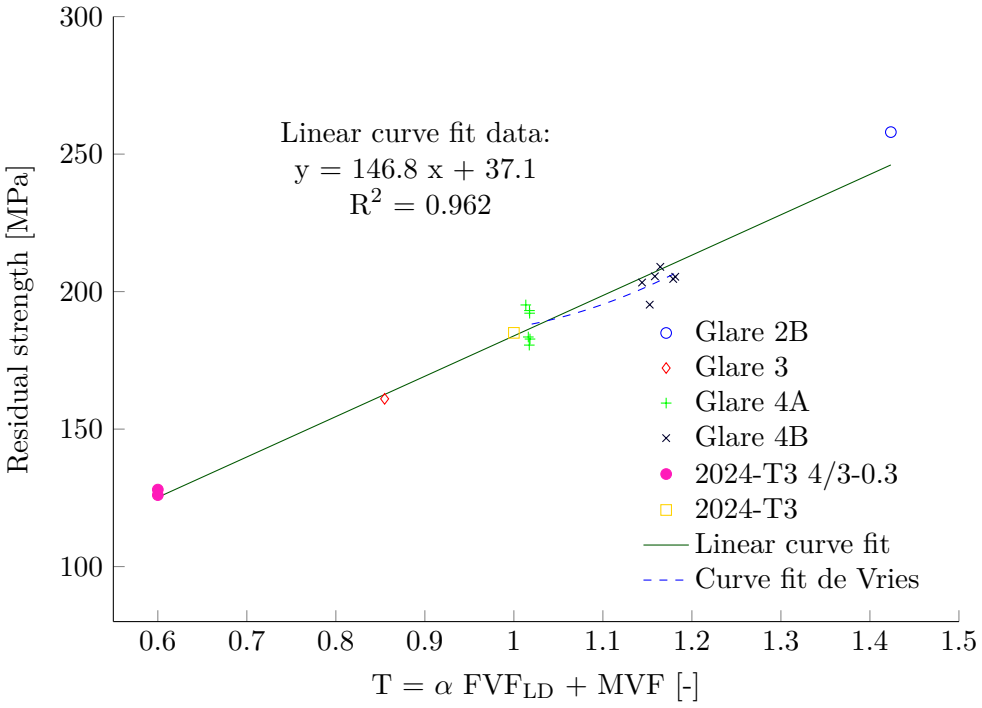

Figure A.2: Residual strength as function of T in T-L direction [18, 23].

Appendix B

Test sample production data

In this appendix all data corresponding to the test samples is given. Including for every sample a C-scan image and precise measurement of the critical dimensions. The appendix is ended with an overall view of the used test set-up.

B.1 Panel design

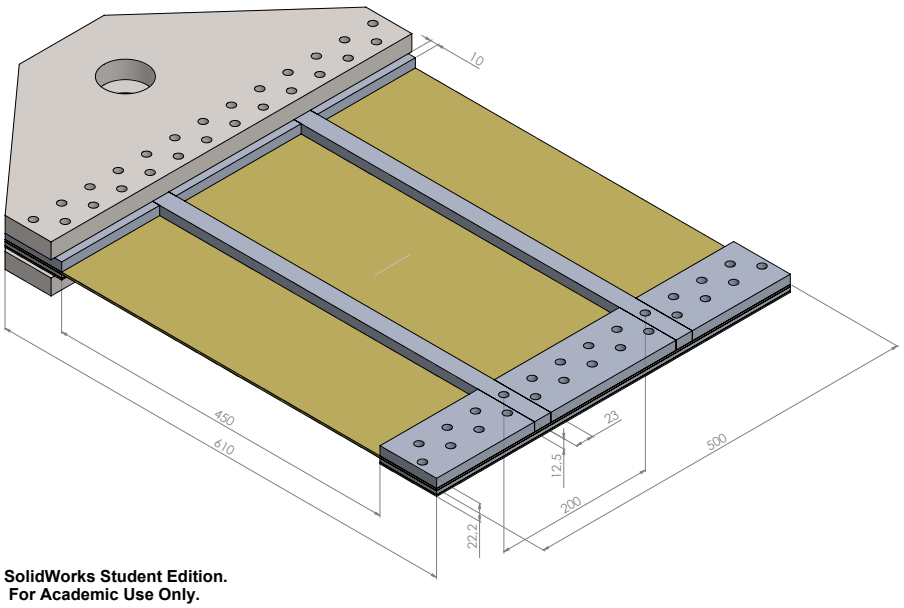

Figure B.1: Isometric view of the developed test sample.

B.2 Metal pretreatment procedure

This section describes the production steps in detail taken during the development of the test specimens. All steps are executed at the Department of Aerospace Structures and Material Laboratory located at the TU Delft and follow a procedure similar to that of ASTM 3933-98 [54].

Function related to the different processes:

Cleaning
Removing any contamination of grease of the surface

Etching
Removal of the aluminium oxide layer created at the surface
Formation of a new controlled oxide layer

Anodising
Increasing the porosity created at the surface
Increasing the porosity depth

Primer
Protecting the carefully created surface
Improve the wetting of the adhesive
Improve corrosion resistance

Procedure described per step:

1. Cleaning step
   (a) Before any handling the specimens should be thoroughly cleaned using acetone to remove any grease or contamination on the surface
   (b) The specimen is dimpled in an alkaline bath for 6 minutes by hanging the parts using Nylon threads. The bath contains a caustic solution of sodium hydroxide (175 $gr./L$ at room temperature)
   (c) Next the specimen is rinsed to remove any sodium oxide attached to the specimen. Therefore it is dimpled in a clean water bath for 2-3 minutes.
2. Etching step
   (a) After the specimen is rinsed in clean water the etching process is started. Therefore the specimen is de-oxidized, by dimpling in a bath containing a nitric acid solution for 6 minutes. The content of the bath is a solution of nitric acid and water in a ratio of 1 : 1.
   (b) Subsequently the specimen is rinsed again.

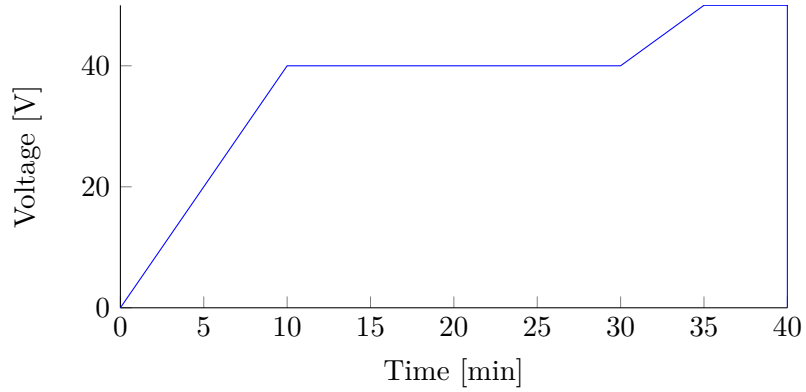

Figure B.2: Applied voltage envelope during anodising.

3. Anodising step

   (a) Once the specimen has been cleaned and etched, the anodising procedure can be started. Therefore the anodising bath is heated to $40°C \pm 2°C$. The specimen is clamped to the anode using a titanium clamp. Subsequently the voltage is increased following the profile given Figure B.2. This results in a changing current in the product, giving an indications of the created oxide layer.

   (b) After the anodising process is finished the product is cleaned above the anodising bath with demi-water to remove any excessive chromatic acid and dimpled in a clean water bath to remove all fluids.

   (c) The anodising is finished with drying the specimen for at least an hour.

4. Primer step

   (a) To protect the carefully created surface the specimen is primed using Cytec BR 127 [55] and should be dried for at least 30 minutes.

   (b) When the primer has been applied, it should be cured in the oven at $120°C \pm 6°C$ for a minimum of 30 minutes.

B.3 Test sample analysis results

B.3.1 Ultrasonic C-scan results

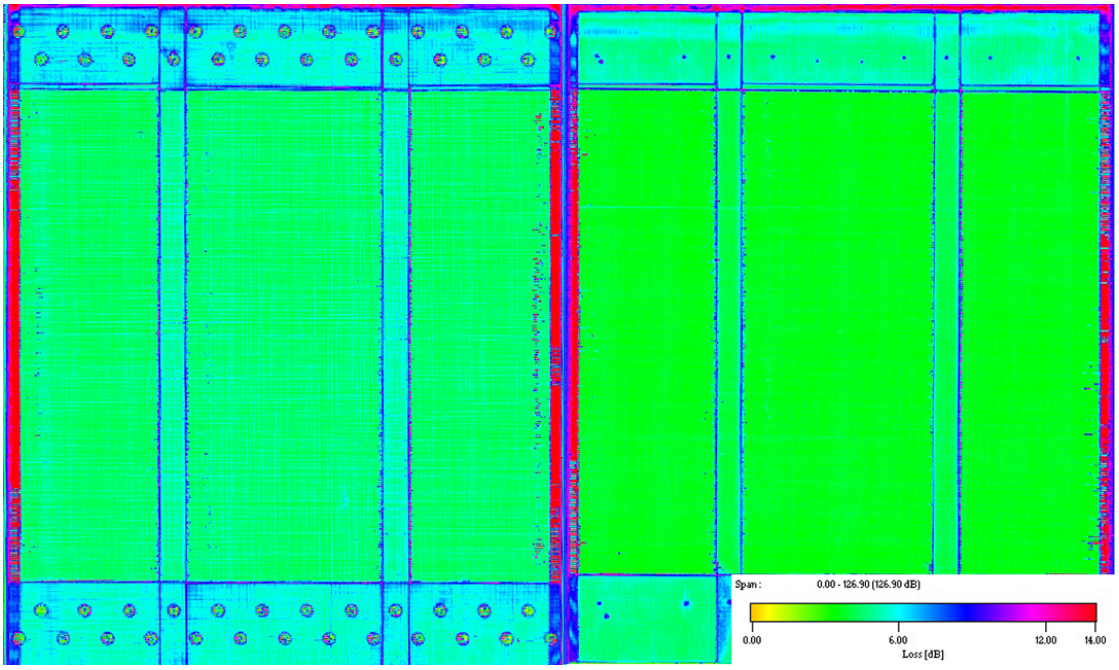

Figure B.3: C-scan image of test sample 1 and 4.

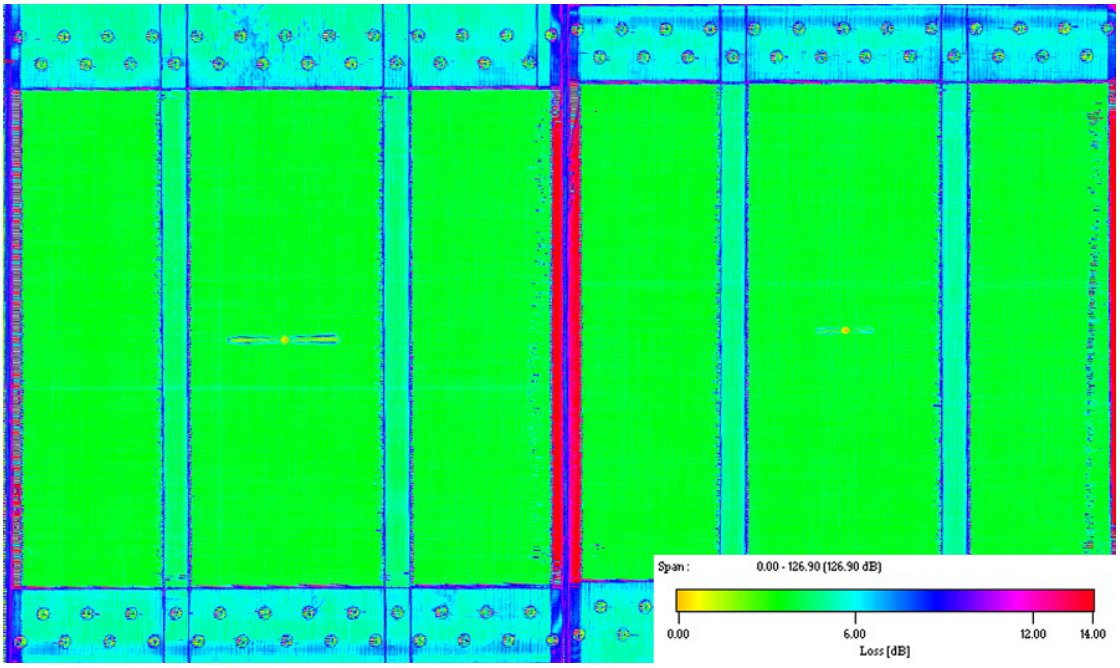

Figure B.4: C-scan image of test sample 2 and 3.

B.3.2 Test samples measurement data

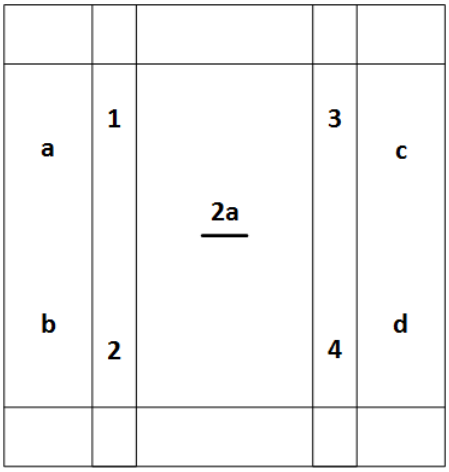

Figure B.5: Locations of measurements.

Table B.1: Measured dimension all in millimetres.

Skin thickness (t)	Panel 1	Panel 2	Panel 3	Panel 4
a	2.672	2.686	2.673	2.680
b	2.678	2.680	2.685	2.688
c	2.686	2.700	2.680	2.686
d	2.695	2.675	2.683	2.683
Average	2.683	2.685	2.680	2.684
Stiffener width (w_{st})	Panel 1	Panel 2	Panel 3	Panel 4
1	23.20	23.08	22.95	22.91
2	23.27	22.81	23.12	22.76
3	23.10	23.08	23.10	22.86
4	22.90	23.04	23.10	23.05
Average	23.12	23.00	23.07	22.90
Initial crack length ($2a$)	Panel 1	Panel 2	Panel 3	Panel 4
Front	39.38	100.14	49.94	19.21
Back	39.27	99.85	49.85	19.06
Average	39.33	100.00	49.90	19.14

B.4 Test set-up

Figure B.6: General view of the test set-up used.

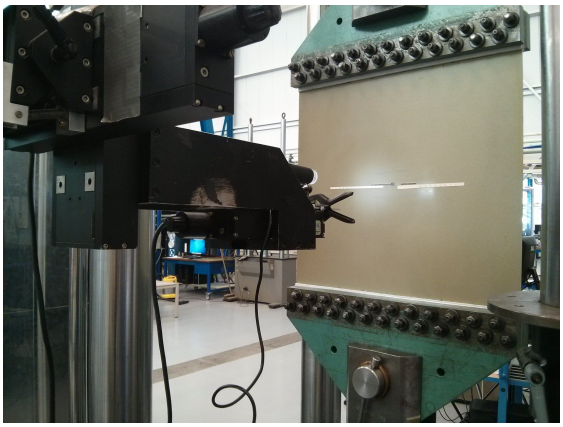

Figure B.7: Close-up of the crack length measuring microscope set-up.

Appendix C

Model validation

The remainder of the residual strength curve obtained with the prediction method are given in this appendix. Consisting of flat plate results for respectively Glare 3 T-L and Glare 4B L-T and a stiffened structure made of Glare 3 3/2 0.3 with Glare 2 2/1 0.2 doubler.

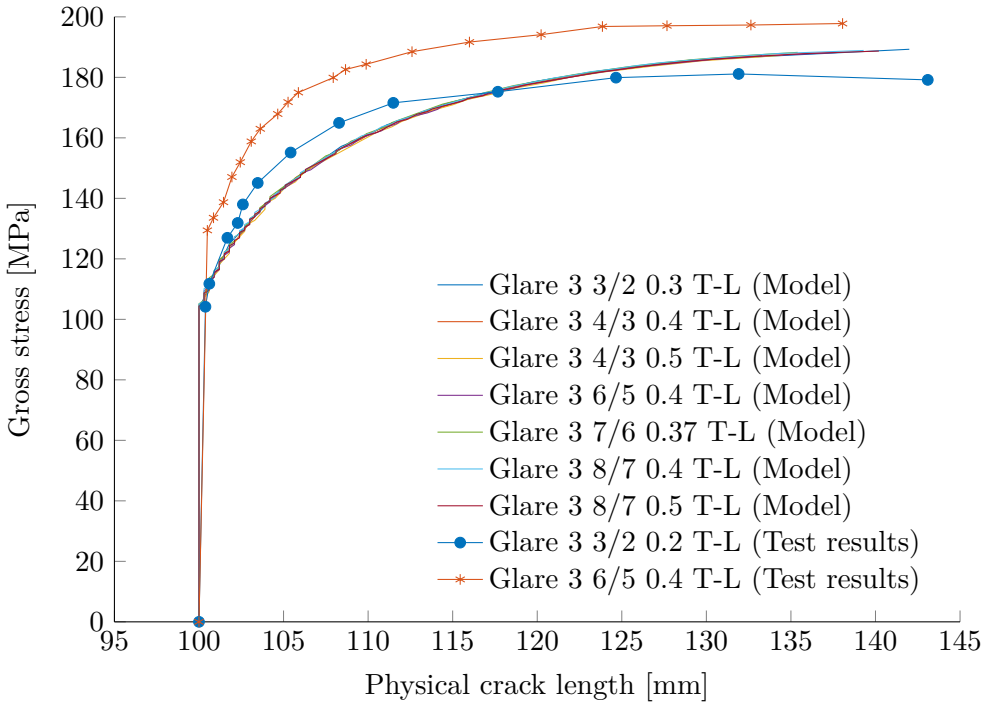

Figure C.1: Comparison between experimental and predicted results for several Glare 3 T-L grades, $W = 800\ mm$ and $2a/W = 0.25$ [40].

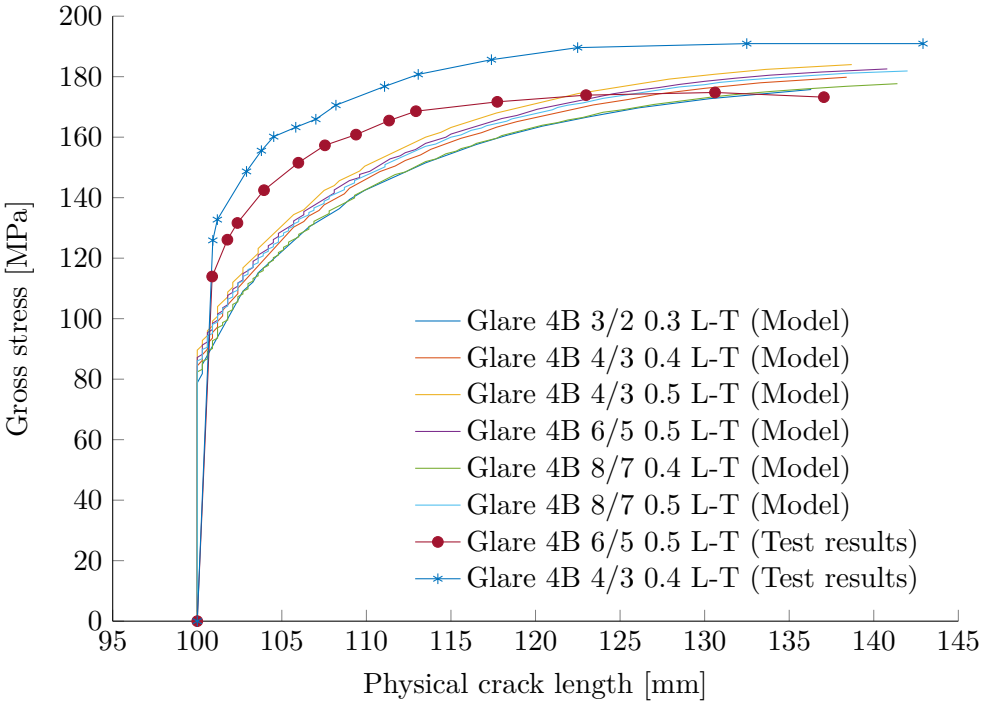

Figure C.2: Comparison between experimental and predicted results for several Glare 4B L-T grades, $W = 800\ mm$ and $2a/W = 0.25$ [40].

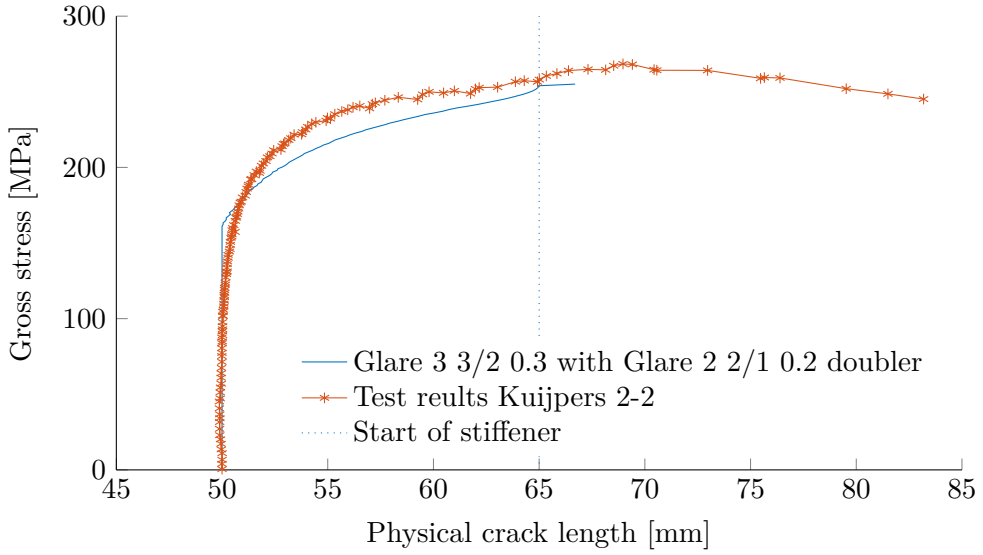

Figure C.3: Bonded panel tested in L-T direction, skin Glare 3 3/2 0.3 and stiffener Glare 2 2/1 0.2. $W_{sk} = 400\ mm$, $W_{st} = 25\ mm$ and $2a/W = 0.25$ [47].

Appendix D

Model input parameters, model prediction and experimental observations

The last appendix contains the model input parameters, remaining figures and observations related to Chapter 5. First the input parameters used in the prediction method are given followed by model predictions of test sample 3 and finalised with the observations done during the testing.

D.1 Model input parameters

Table D.1: Input parameters used in the prediction method [18].

Material property	Aluminium 2024-T3	UD S2 glass fibres	unit
E_x	72	54	GPa
E_y	72	9.4	GPa
μ_{xy}	0.33	0.33	-
μ_{yx}	0.33	$\mu_{xy} * E_y/E_x$	-
G_{xy}	27	5.55	GPa
t	0.34	0.125	mm
$\sigma_{0,2}$	350	-	MPa
σ_c	450	2640	MPa

D.2 Test sample 3 prediction

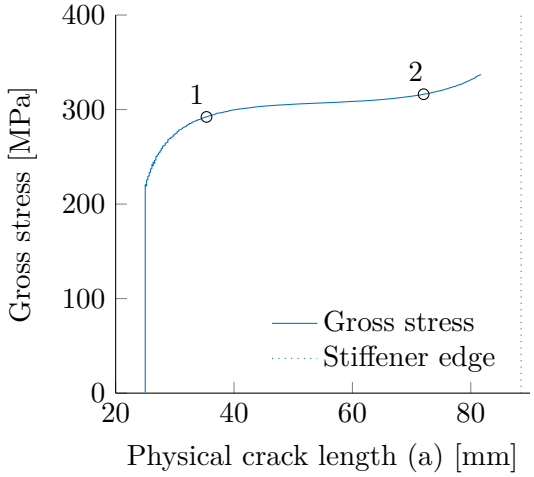

Figure D.1: Residual strength predictions for test sample 3, $2a/W = 0.1$, $W = 500\ mm$.

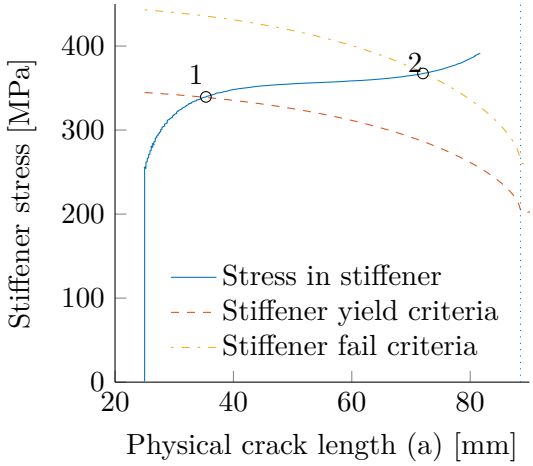

Figure D.2: Stiffener failure determination for test sample 3, $2a/W = 0.1$, $W = 500\ mm$.

D.3 Test observations

During the tests, observations are done, which may relate to a deviation in the obtained test results. It is important that they are documented for further post processing.

- The stiffener contour is visible on the flat side of the sample, indicating that the sample may not be entirely flat any more.
- During all tests out of plane displacement of the crack flanks was identified, as can be seen in Figure D.3.
- The crack passed the stiffener for test sample 1 and 3 without failure of the complete sample. This crack region could only be observed on the back side of the panel, implying a non through-the-thickness crack.
- The stiffener of test sample 1 and 4 immediately failed at the location of the bolt, after unstable crack growth of the panel, probably caused by net section yielding.
- After all tests a large delamination area could be identified at the stiffener edge

Figure D.3: Out of plane displacement observed during testing.